Journal of
Nanoscience and Nanotechnology
Vol. 7, 1197–1220, 2007

Studying Single-Wall Carbon Nanotubes Through Encapsulation: From Optical Methods Till Magnetic Resonance

Ferenc Simon†

Institut für Materialphysik, Universität Wien Strudlhofgasse 4, A-1090 Wien, Austria

Encapsulating fullerenes, magnetic fullerenes, ^{13}C isotope enriched fullerenes, and organic solvents inside SWCNTs enables to yield unprecedented insight into their electronic, optical, and interfacial properties and to study SWCNT growth. In addition to customary methods of their studies such as e.g., optical absorption or Raman spectroscopy, these efforts enables to employ electron spin resonance (ESR) and nuclear magnetic resonance (NMR) spectroscopy. Encapsulated C_{60} fullerenes are transformed to inner tubes by a high temperature annealing. The diameter distribution of the inner tubes follow that of the outer ones and their unique, low defect concentration makes them an ideal model system for high resolution and energy dependent Raman studies. The observation of Raman modes of individual inner-outer tube pairs allows to measure the inner-outer tube interaction strength that is also well described theoretically. Reversible closing and opening of SWCNT can be studied in a diameter selective manner by encapsulating C_{60} and transforming it to an inner tube. The growth of inner tubes can be achieved from ^{13}C enriched encapsulated organic solvents, which shows that the geometry of the fullerene does not play a particular role in the inner tube growth as it was originally thought. In addition, it opens new perspectives to explore the in-the-tube chemistry. Growth of inner tubes from ^{13}C enriched fullerenes provides a unique isotope engineered heteronuclear system, where the outer tubes contain natural carbon and the inner walls are controllably ^{13}C isotope enriched. The material enables to identify the vibrational modes of inner tubes which otherwise strongly overlap with the outer tube modes. The ^{13}C NMR signal of the material has an unprecedented specificity for the small diameter SWCNTs. Temperature and field dependent ^{13}C T_1 studies show a uniform metallic-like electronic state for all inner tubes rather than distributed metallic and isolating behavior. A low energy, 3 meV gap is observed that is tentatively assigned to a long sought Peierls transition in the small diameter SWCNTs. Encapsulating magnetic fullerenes, such as N@C_{60} and C_{59}N opens the way for local probe ESR studies of the electronic properties of the SWCNTs.

Keywords: Carbon Nanotubes, Fullerene Encapsulation, Double-Wall Carbon Nanotubes, Isotope Engineered Nanotubes, Raman Spectroscopy, Magnetic Resonance Spectroscopy.

CONTENTS

1. INTRODUCTION

The nano-era can be originated from the discovery of carbon nanotubes (CNTs) by Sumio Iijima in 1991.[1] Before 1991, nanoscience and nanotechnology usually

---

[†] Present address: Budapest University of Technology and Economics, Institute of Physics and Solids in Magnetic Fields Research Group of the Hungarian Academy of Sciences, H-1521, Budapest P.O. Box 91, Hungary.

meant small clusters of atoms or molecules with seemingly of fundamental interest only. The originally discovered multi-wall CNTs were soon followed by the discovery of single-wall CNTs,[2, 3] which are both believed to be of paramount importance for applications. The principal interest in CNTs comes from the fact that they contain carbon only and all carbons are locally sp^2 bound, like in graphite, which provides unique mechanical and transport properties. This, combined with their huge, >1000, aspect ratio (the diameters being 1–20 nm and their lengths over 1 micron), endows them with their enormous application potential. The not exhaustive list of applications includes field-emission displays (exploiting their sharp tips),[4] cathode emitters for small sized X-ray tubes for medical applications,[5] reinforcing elements for CNT-metal composites, tips for scanning probe microscopy,[6] high current transmitting wires, cables for a future space elevator, elements of nano-transistors,[7] and elements for quantum information processing.[8]

Carbon nanotubes can be represented as rolled up graphene sheets, i.e., single layers of graphite. Depending on the number of coaxial carbon nanotubes, they are usually classified into multi-wall carbon nanotubes (MWCNTs) and single-wall carbon nanotubes (SWCNTs). Some general considerations have been clarified in the past 14 years of nanomaterial research related to these structures. MWCNTs are more homogeneous in their physical properties as the large number of coaxial tubes smears out individual tube properties. This makes them suitable candidates for applications where their nanometer size and the conducting properties can be exploited such as e.g., nanometer sized wires. In contrast, SWCNT materials are grown as an ensemble of weakly interacting tubes with different diameters. The physical properties of similar diameter SWCNTs can change dramatically as the electronic structure is very sensitive on the rolling-up direction, the so-called chiral vector.[9, 10] The chiral vector is characterized by the (n,m) vector components which denote the direction along which a graphene sheet is rolled up to form a nanotube. Depending on the chiral vector, SWCNTs can be metallic or semiconducting.[10] This provides a richer range of physical phenomena as compared to the MWCNTs, however significantly limits the range of applications. To date, neither the directed growth nor the controlled selection of SWCNTs with a well defined chiral vector has been performed successfully. Thus, their broad applicability is still awaiting. Correspondingly, current research is focused on the post-synthesis separation of SWCNTs with a narrow range of chiralities[11–14] or on methods which yield information that are specific to SWCNTs with different chiralities. Examples for the latter are the observation of chirality selective band-gap fluorescence in semiconducting SWCNTs[15] and chirality assigned resonant Raman scattering.[16, 17]

Clearly, several fundamental questions need to be answered before all the benefits of these novel nanostructures could be fully exploited. Recent theoretical and experimental efforts focused on the understanding of the electronic and optical properties of single-wall carbon nanotubes. It has been long thought that the one-dimensional structure of SWCNTs renders their electronic properties inherently one-dimensional.[9, 10] This was suggested to result in a range of exotic correlated phenomena such as the Tomonaga-Luttinger (TLL) state,[18] the Peierls transition,[19, 20] ballistic transport,[21] and bound excitons.[22–25] The presence of the TLL state is now firmly established,[26–28] there is evidence for the ballistic transport properties[21] and there is growing experimental evidence for the presence of excitonic effects.[29, 30] The Peierls transition, however remains still to be seen.

An appealing tool to study the SWCNT properties originates from the discovery of fullerenes encapsulated inside SWCNTs by Smith, Monthioux, and Luzzi.[31] This peapod structure is particularly interesting as it combines two fundamental forms of carbon: fullerenes and carbon nanotubes. A high-resolution transmission electron microscopy (HR-TEM) image of a peapod is shown in Figure 1. It was also shown that macroscopic filling with the fullerenes can be achieved.[32, 33] This, in principle, opens the way to encapsulate magnetic fullerenes which would enable the study of the tube electronic properties using electron spin resonance as it is discussed in this review. Another interesting follow-up of the peapod structure discovery is that the encapsulated fullerenes can be fused into a smaller diameter inner tube[34, 35] thus producing a double-wall carbon nanotube (DWCNT). DWCNTs were first observed to form under intensive electron radiation[32] in a high resolution transmission electron

Ferenc Simon has been Assistant Professor at the Budapest University of Technology and Economics, Hungary since 2005. His current research focuses on the magnetic resonance studies of novel nanostructured materials. Dr. Simon was born on 8th June, 1974 in Budapest. He obtained his Ph.D. degree for "Magnetic resonance studies of strongly correlated electron systems" in 2002 in the group of Professor András Jánossy. In 2003, he joined the group of Professor Hans Kuzmany at the University of Vienna, Austria and was employed as a Marie-Curie Research Fellow with an individual Intra-European fellowship until 2005. He made contributions to the optical and magnetic resonance spectroscopy of superconductors, antiferromagnets and single-wall carbon nanotubes and also to the isotope engineered synthesis of carbon nanotubes. In 2006 he received the "Talentum Prize of the Hungarian Academy of Sciences."

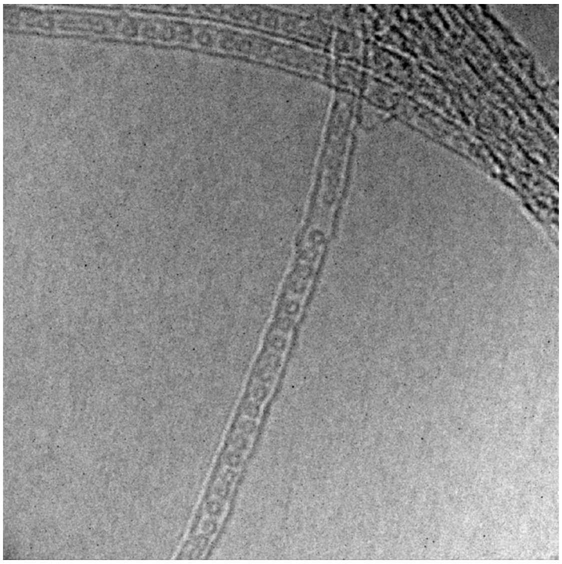

Fig. 1. HR-TEM image of C_{60}@SWCNT peapods.

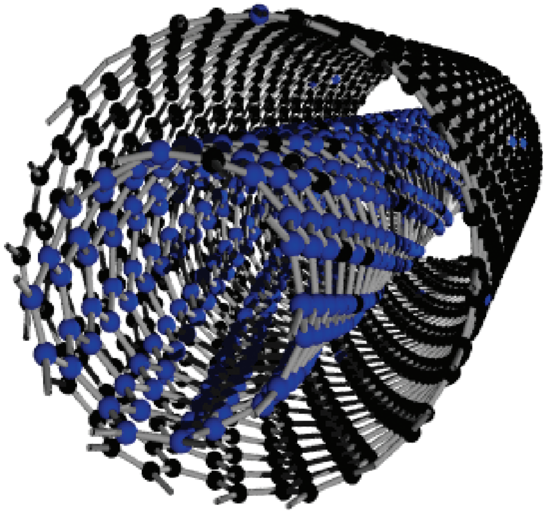

Fig. 2. Schematic structure of an isotope engineered DWCNT with (14,6) outer and (6,4) inner tubes. ^{12}C and ^{13}C are shown in black and blue, respectively. The inner tube is 89% ^{13}C enriched and the outer contains natural carbon (1.1% ^{13}C abundance), which are randomly distributed for both shells.

microscope from C_{60} peapods. Following the synthesis of C_{60} peapods in macroscopic amounts,[33] bulk quantities of the DWCNT material are available using a high temperature annealing method.[35] Alternatively, DWCNTs can be produced with usual synthesis methods such as arc-discharge[36] or CVD[37] under special conditions. According to the number of shells, DWCNTs are between SWCNTs and MWCNTs. Thus, one expects that DWCNTs may provide a material where improved mechanical stability as compared to SWCNTs coexists with the rich variety of electronic properties of SWCNTs. There are, of course, a number of yet unanswered questions e.g., if the outer tube properties are unaffected by the presence of the inner tube or if the commensurability of the tube structures plays a role. These questions should be answered before the successful application of these materials.

The inner tubes grown inside SWCNTs from peapods turned out to be a particularly interesting system as they are remarkably defect free which results in very long phonon life-times, i.e., very narrow vibrational modes.[38] In addition, their smaller diameters results in a larger energy spread, i.e., larger spectral splitting, for diameter dependent phonon modes such as e.g., the radial breathing mode (RBM). These two effects make the inner tubes very suitable to study diameter dependent physics of the small diameter tubes with precision. Here, we review how to employ the inner tubes as *probes* of the outer tube properties. The additional benefit of the inner tube growth from fullerenes is that the starting carbon source can be tailored at wish, e.g., when ^{13}C isotope enriched fullerenes are encapsulated inside the SWCNT host tubes, ^{13}C isotope enriched inner tubes are grown. In Figure 2 we show the schematics of such a DWCNT.

Here, we review the efforts to study the SWCNTs properties through encapsulation using Raman and magnetic resonance spectroscopy. The reviewed phenomena include the precise characterization of diameter distribution of SWCNTs, the study of reversible hole engineering on the SWCNTs, study of the inner tube growth mechanism with the help of ^{13}C isotope labeling, the study of local density of states on the tubes using nuclear magnetic resonance (NMR) on the ^{13}C isotope enriched inner tubes, and the electron spin resonance (ESR) studies of the SWCNTs using encapsulated magnetic fullerenes. This review is organized as follows. First, we present the general properties of DWCNTs using Raman, discuss the electronic and vibrational properties of the inner tubes, which are the probes in the subsequent studies. Second, we present the use of the inner tubes to probe the host outer tube diameter distribution and to study the opening and closing of holes on the outer tubes. Third, we present a study on the inner tube growth mechanism using isotope enriched carbon. Fourth, we discuss the NMR results on the isotope enriched inner tubes and in particular we present the observation of a low energy spin-gap in the density of states of SWCNTs. Fifth, we discuss the efforts related to studying the SWCNT properties by encapsulating magnetic fullerenes using ESR.

2. EXPERIMENTAL METHODS AND SAMPLE PREPARATION

2.1. Sample Preparation

2.1.1. The Starting SWCNT Samples

SWCNTs from different sources and prepared by different methods were used in the studies described. Arc-discharge grown SWCNTs with 50% supplier provided weight purity were purchased from Nanocarblab (Nanocarblab, Moscow, Russia) and laser ablation prepared SWCNTs with 10% weight purity were purchased from Tubes@Rice (Tubes@Rice, Houston, USA). This latter material was purified through repeated steps of air oxidation and washing in HCl. Some laser ablation prepared and purified samples were obtained from Kataura. The purified samples are usually well opened to enable fullerene encapsulation. If not, annealing in air at 450 °C for 0.5 hour makes them sufficiently open. The HiPco samples used as reference were purchased from CNI (Carbon Nanotechnologies Inc., Houston, USA). Most samples were used in the form of a buckypaper, which is prepared by filtering a suspension of SWCNTs. We found that commercially available SWCNTs already meet a required standard in respect of purity and quality. In addition, for the amount of experimental work described here, reproducible samples i.e., a large amount of SWCNTs from similar quality, were required. The commercial samples can meet this requirement, which compensates for their slightly inferior quality as compared to laboratory prepared ones.

2.1.2. Synthesis of Peapods

Encapsulation of fullerenes at low temperatures inside SWCNTs (solvent method) was performed by sonicating the fullerene and opened SWCNT suspensions together in organic solvents following Refs. [39–42]. For fullerene encapsulation at high temperatures (the vapor method), the SWCNTs and the fullerenes were sealed under vacuum in a quartz ampoule and annealed at 650 °C for 2 hours.[33] Fullerenes enter the inside of the SWCNTs at this temperature due to their high vapor pressure that is maintained in the sealed environment. Non-encapsulated fullerenes were removed by dynamic vacuum annealing at the same temperature for 1 hour. High purity fullerenes were obtained from a commercial source (Hoechst AG, Frankfurt, Germany). The filling of SWCNTs with the fullerenes was characterized by observing the peapod structure in high-resolution transmission electron microscopy (HR-TEM), by X-ray studies of the one-dimensional array of fullerenes inside the SWCNTs and by the detection of the fullerene modes from the cages encapsulated inside the SWCNTs using Raman spectroscopy.[33, 43]

2.1.3. Synthesis of DWCNTs

DWCNTs were prepared by two routes: from fullerene peapods and using chemical vapor deposition (CVD) growth technique.[44] The peapods were transformed to DWCNTs by a dynamic vacuum treatment at 1250 °C for 2 hours following Ref. [35]. Again, the DWCNT transformation was followed by HR-TEM and by the observation of the DWCNT structure factors using X-ray studies. In addition, new Raman modes emerge after the 1250 °C heat treatment particularly in a frequency range that is clearly upshifted from the outer tube RBMs.

For the CVD DWCNT growth, the catalyst was a modified version of the Fe/Mo/MgO system developed by Liu et al.[45] for SWCNT synthesis. The catalyst possessed a molar Fe : Mo : MgO ratio of 1 : 0.1 : 110. Nanotubes were synthesized in a fixed bed horizontal quartz tube reactor. The gas stream was a C_2H_2 : Ar (10 cm^3/min : 150 cm^3/min volumetric flow rate at ambient temperature and pressure) reaction mixture. The reactor was pushed into the furnace and kept there at 850 °C for 20 minutes. The catalyst was removed from the sample by dissolving in excess of concentrated HCl solution at room temperature. The remaining carbonaceous material was filtered and washed with distilled water and dried at 120 °C.

Both kinds of DWCNTs have certain advantageous and disadvantageous properties. For peapod template grown DWCNTs, the inner tube is known to fill only up to $\sim 70\%$ of the outer tube length.[46] This is the consequence of insufficient carbon in the fullerenes: the C_{60} peapods have 60 carbon atoms per 1 nm (the lattice constant of the peapod) whereas the (9,0) inner tube with $d = 0.7084$, which is representative of the most abundant 7 nm diameter inner tube contains 36 carbon atoms per the $c_0 = 0.4238$ nm lattice constant.[47] In contrast, CVD grown inner tubes fill up to the total length of the outer tubes, however such samples have usually a less well defined tube diameter distribution due to the inevitable growth of small diameter SWCNTs and large diameter DWCNTs.[48] Peapod template grown DWCNTs can be grown with relatively narrow diameter distribution due to the available narrow diameter distribution of the SWCNT host tubes. This also allows for a good control over the DWCNT diameter as described in Ref. [49] and is discussed below.

2.1.4. Synthesis of Isotope Engineered DWCNTs

Commercial ^{13}C isotope enriched fullerenes (MER Corp., Tucson, USA) were used to prepare fullerene peapods C_{60},C_{70}@SWCNT with enriched fullerenes. Two supplier specified grades of ^{13}C enriched fullerene mixtures were used: 25 and 89%, whose values were slightly refined based on the Raman spectroscopy. The 25% grade was nominally C_{60}, and the 89% grade was nominally C_{70} with C_{60}/C_{70}/higher fullerene compositions of 75 : 20 : 5 and 12 : 88 : <1, respectively. The above detailed standard routes were performed for the peapod and the DWCNT productions.

2.2. Raman Spectroscopy

Raman spectra were measured with a Dilor xy triple spectrometer using various lines of an Ar/Kr laser, a He/Ne laser and a tunable Ti : sapphire and Rhodamin dye-laser in the 1.54–2.54 eV (805–488 nm) energy range. Tunable lasers allow to record the so-called Raman map[16, 17] i.e., to detect the SWCNT resonance energies through the Raman resonance enhancement,[50] which ultimately allows the chiral index assignment. The spectra can be recorded in normal (NR) and high resolution (HR) mode, respectively

($\Delta\bar{\nu}_{\text{NR}} = 1.3$ cm^{-1} for blue and $\Delta\bar{\nu}_{\text{HR}} = 0.4$ cm^{-1} in the red). The samples in the form of bucky-paper are kept in dynamic vacuum and on a copper tip attached to a cryostat, which allows temperature variation in the 20–600 K temperature range. Raman spectroscopy was used to characterize the diameter distribution of the SWCNTs, to determine the peapod concentrations, and to monitor the DWCNT transformation of the peapod samples.

2.3. Nuclear Magnetic Resonance

Nuclear magnetic resonance (NMR) is usually an excellent technique for probing the electronic properties at the Fermi level of metallic systems. The examples include conducting polymers, fullerenes, and high temperature superconductors. However the 1.1% natural abundance of ^{13}C with nuclear spin $I = 1/2$ limits the sensitivity of such experiments. As a result, meaningful NMR experiments has to be performed on ^{13}C isotope enriched samples. NMR data were taken with the samples sealed in quartz tubes filled with a low pressure of high purity Helium gas.[51] We probed the low frequency spin dynamics (or low energy spin excitations, equivalently) of the inner-tubes using the spin lattice relaxation time, T_1, defined as the characteristic time it takes the ^{13}C nuclear magnetization to recover after saturation. The signal intensity after saturation, $M(t)$, was deduced by integrating the fast Fourier transform of half the spin-echo for different delay times, t.

2.4. Electron Spin Resonance

The peapod and the reference SWCNT materials were mixed with the ESR silent high purity SnO$_2$ in a mortar to separate the pieces of the conducting bucky-papers. The samples were sealed under dynamic vacuum. A typical microwave power of 10 μW and 0.01 mT magnetic field modulation at ambient temperature were used for the measurements in a Bruker Elexsys X-band spectrometer.

3. RESULTS AND DISCUSSION

3.1. Inner Tubes in DWCNTs as Local Probes

3.1.1. Electronic and Vibrational Properties of DWCNTs

Encapsulating fullerenes and their transformation into inner tubes by the high temperature annealing process[35] provides a unique opportunity to study the properties of the host outer tubes. In Figure 3 we show the evolution of the SWCNT Raman spectrum upon C$_{60}$ fullerene encapsulation and the DWCNT transformation after Ref. [38]. The series of sharp modes in the peapod spectrum, which are related to the encapsulated fullerenes,[43] disappear upon the heat treatment and a series of sharp modes appear in the 250–450 cm^{-1} spectral range. The presence of inner tubes after this protocol have been independently confirmed by HR-TEM[34] and structures similar to that shown in Figure 4 were observed. The small diameter tubes with $d \sim 0.7$ nm would have RBM modes in the ~250–450 cm^{-1} spectral range, which clarifies the identification of these modes. The identification of the inner tube RBMs is possible due to the strong d dependence of this Raman mode.[52] Assignment of less diameter dependent modes such as the G mode[10] to inner and outer tubes are more difficult although a number of small intensity new modes are observed for the DWCNT sample in Figure 3. It is shown in Section 3.2 that unambiguous assignment can be given with the help of selective isotope enrichment of the inner walls.

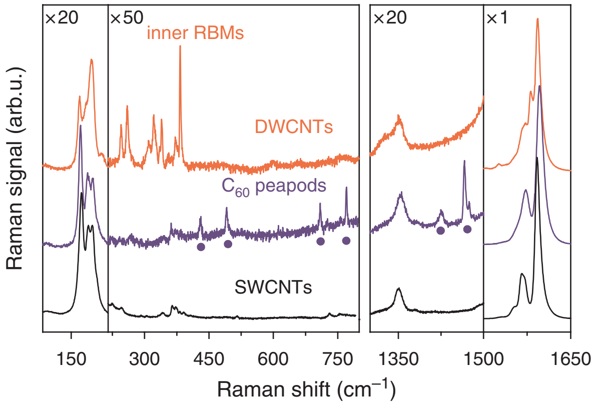

Fig. 3. Transformation of fullerene peapods to DWCNTs as followed with Raman spectroscopy at 496.5 nm laser excitation and 90 K. The SWCNT Raman spectra (lower curve) is shown as reference. The fullerene related peapod modes (dots) in the middle curve disappear upon the heat treatment. Note the sharp RBMs appearing in the 250–450 cm^{-1} for the DWCNT sample.

The assignment of the dispersive SWCNT G′ mode[10] mode to inner and outer tube modes was also possible due to the (weaker) diameter dependence and the high energy of this mode.[54] In Figure 5, we show this mode for

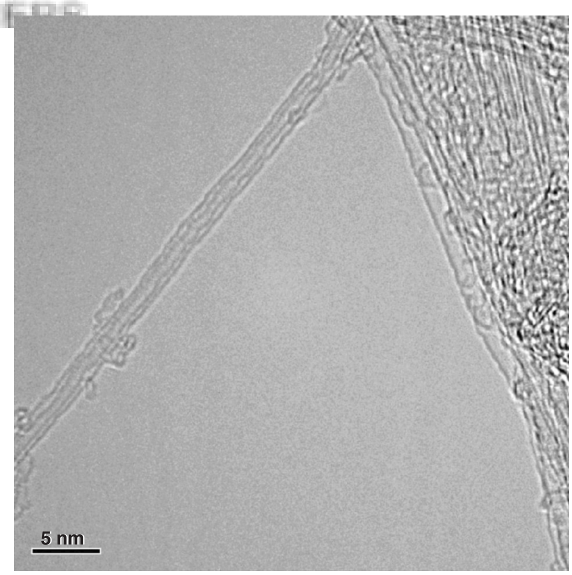

Fig. 4. HR-TEM micrograph of a peapod template based DWCNT.

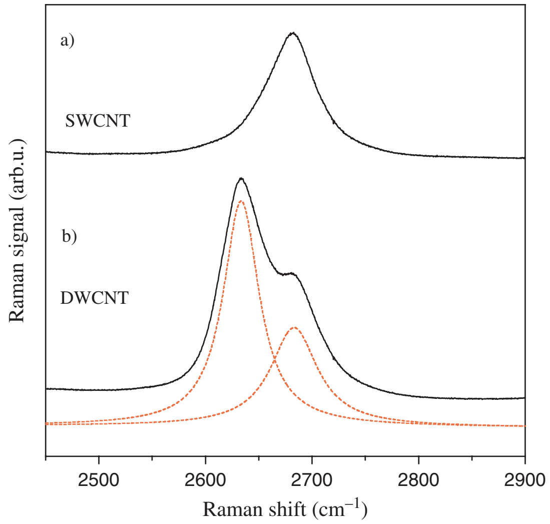

Fig. 5. Raman spectra in the G′ mode range of (a) SWCNT and (b) DWCNT samples at DWCNT 515 nm laser excitation. Dashed curves shows deconvolution to inner (lower frequency) and outer (higher frequency) tubes. Reprinted with permission from [53], R. Pfeiffer et al., *Phys. Rev. B* 71, 155409 (**2005**). © 2005, American Physical Society.

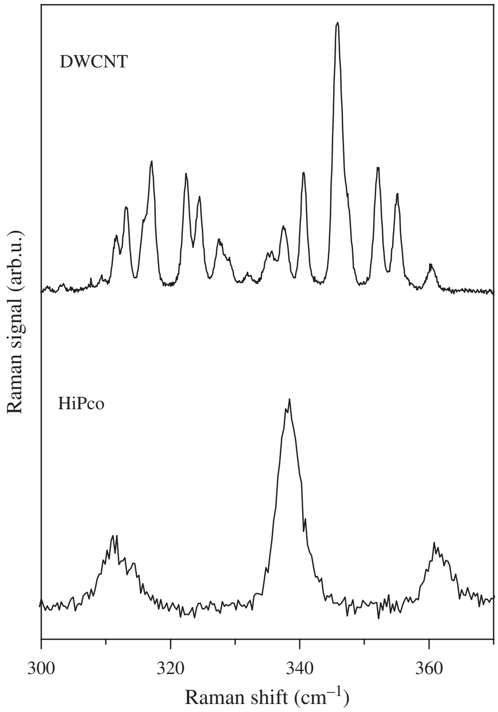

Fig. 6. Raman spectra of the RBMs in DWCNT and HiPco (SWCNT) samples at 594 nm laser excitation and 90 K in the high resolution spectrometer mode.

DWCNTs. Clearly, the DWCNT G′ mode consists of two components. Other modes, such as the SWCNT D and G modes are less diameter sensitive and assignment of inner and outer tube D and G modes requires the use of isotope enriched DWCNTs as shown below.

A variety of additional information can be gained about the inner tube properties when their RBMs are studied using the additive mode, i.e., high-resolution of the Raman spectrometer. In Figure 6, we show the inner tube RBMs at 90 K with high-resolution in comparison with an SWCNT sample with similar tube diameter prepared by the HiPco process. Three striking observations are apparent in the comparison of the two spectra:
(i) there are a larger number of inner tube RBMs than geometrically allowed and they appear to cluster around the corresponding modes in the SWCNT sample,
(ii) the inner tube RBMs are on average an order of magnitude narrower than the SWCNT RBMs in the HiPco sample[38] and
(iii) the Raman intensity of the inner tubes is large in view of the ~3 times less number of carbon atoms on them.[54]

Points (ii) and (iii) are explained by the long phonon and quasi-particle life-times of inner tubes which are discussed further below.

Observation (i), i.e., the clustering behavior of the observed inner tube RBMs around SWCNT RBMs, is further evidenced in energy dispersive Raman measurements. In Figure 7, we show the Raman map for the DWCNTs from Ref. [55]. The advantage of studying Raman maps is that the optical transition energies are also contained in addition to the Raman shifts. These two quantities uniquely identify the chirality of a nanotube.[10,56,57] The analogous Raman map for HiPco SWCNTs were measured by Fantini et al.[16] and Telg et al.[17] Their results are also shown in Figure 7 with squares and circles for metallic and semiconducting tubes, respectively. It turns out that family

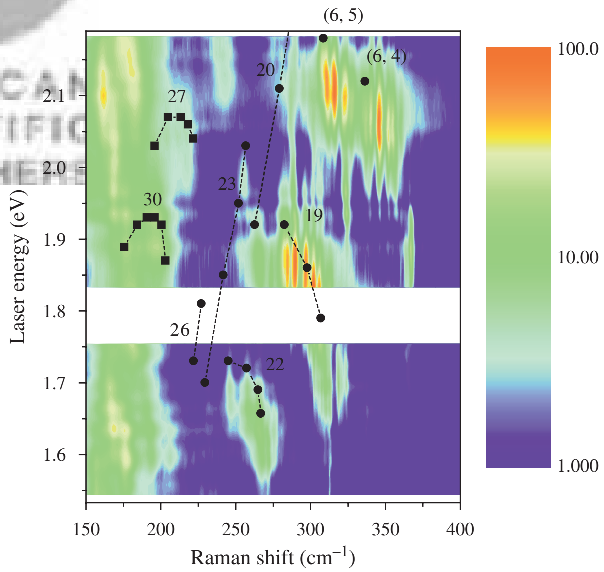

Fig. 7. Raman map of DWCNTs. Circles and squares are the E_{22}^{s} and E_{11}^{m} peaks as measured in a HiPco sample 16, respectively. The family numbers and the chiral indexes for the (6,5) and (6,4) tubes are indicated. Dashed lines join chiralities in the same family. Laser excitation was not available in the missing area. Reprinted with permission from [55], R. Pfeiffer et al., *Phys. Rev. B* 72, 161404 (**2005**). © 2005, American Physical Society.

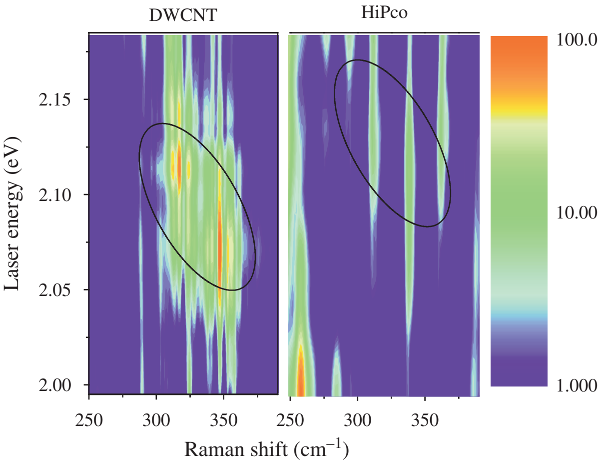

Fig. 8. Raman map comparison of the (6,5) and (6,4) tube RBM ranges for DWCNT and SWCNT (HiPco) samples. Ellipsoids indicate the corresponding tube modes. Note the progressive transition energy downshift for the split components of the inner tubes and the 30 meV transition energy difference between the two kinds of samples, which are discussed in the text.

patterns with $2n+m=$ const can be identified for which the tube resonance energies and Raman shifts are closely grouped together.[15] The comparison of the HiPco results and the DWCNT Raman map confirms the above statement, i.e., that a number of inner tube modes are observed for the DWCNT where only a few (or one) SWCNT chirality is present. This is best seen for the (6,5) and (6,4) chiralities which are well resolved from other modes.

In Figure 8, we show the Raman maps for the two samples near the energy and Raman shift regions for the (6,5) and (6,4) tube modes.[15–17] The comparison of the Raman maps of the two kinds of samples shows that the corresponding tube modes are split into up to 15 components for the inner tube RBMs. This is explained by the inner-outer tube interaction in the DWCNT samples: an inner tube with a particular chirality can be grown in outer tubes with different diameters (chiralities). The varying inner-outer tube spacing can give rise to a different Raman shift for the split components. The large number of split components is a surprising result as it is expected that an inner tube with a given diameter is grown in maximum 1–2 outer tubes where its growth is energetically preferred.

To further prove the origin of the splitting and to quantify this effect, model calculations on the inner-outer tube interactions were performed[55, 58] following the continuum model of Popov and Henrard[59] that is discussed here. The DWCNT is represented by two nested cylinders with diameters d_i and d_o of the inner and outer shells, respectively. The inner-outer tube interaction is described by the Lennard-Jonnes (LJ) potential: the interaction between two points at a distance r on the two shells is given by

$$V(r) = 4\epsilon[(\sigma/r)^{12} - (\sigma/r)^{6}] \qquad (1)$$

where $\epsilon = 2.964$ meV and $\sigma = 0.3407$ nm are the parametrized values for graphite.[60]

The inner tube RBM frequencies are obtained from the eigenvalues of the DWCNT dynamical matrix written for the RBMs:

$$D = -\frac{1}{\sqrt{m_\mathrm{i} m_\mathrm{o}}} \begin{pmatrix} k_\mathrm{i} + \partial^2\Phi/\partial d_\mathrm{i}^2 & \partial^2\Phi/\partial d_\mathrm{i}\partial d_\mathrm{o} \\ \partial^2\Phi/\partial d_\mathrm{o}\partial d_\mathrm{i} & k_\mathrm{o} + \partial^2\Phi/\partial d_\mathrm{o}^2 \end{pmatrix} \qquad (2)$$

Here m_i and m_o are the masses (per unit length) and k_i and k_o are the force constants of the inner and outer shells, respectively. Φ is the inner-outer tube interaction energy. The force constants can be determined from the RBM frequencies for separate inner and outer SWCNTs using first principles calculations such as in Ref. [52]. The inner-outer tube interaction energy, Φ is a sum of the elastic energies of both tubes and the tube-tube interaction energy, E_LJ:

$$\Phi = Y_1\pi/2[d_{\mathrm{i},0}(\Delta d_\mathrm{i}/d_\mathrm{i})^2 + d_{\mathrm{o},0}(\Delta d_\mathrm{o}/d_\mathrm{o})^2] + E_\mathrm{LJ} \qquad (3)$$

Here $d_{\mathrm{i},0}$ and $d_{\mathrm{o},0}$ are the diameters for separate inner and outer tubes, respectively and Δd_i and Δd_o are their changes in the DWCNTs. $Y_1 = Yd$, $Y = 1.06$ TPa is the graphene in-plane Young's modulus, and $d = 0.335$ nm is the tube wall thickness. The relaxed diameters of the inner and outer tubes are obtained from minimizing the Φ interaction energy.

In Figure 9(a), we show the calculated upshift of the inner tube RBMs for a (6,4) tube as a function of the diameter difference to various outer tubes. Clearly, up to 35 cm^{-1} Raman shift variations can be reproduced. The question remains, however whether such inner-outer tube diameter differences really appear in a sample. In Figure 9(b), we show the assumed Gaussian distribution for the outer tube abundance that was used for the simulation of an inner tube spectrum taking into account the effect of outer tubes. This simulation is shown in Figure 9(c). This procedure assumes equal Raman matrix elements for all members of a cluster which is justified by the inner tube having the same chirality. The calculated frequencies were scaled with a factor of 0.98. To get the best agreement between theory and experiment, the parameters of the Gaussian were $\omega_0 = 348.9$ cm^{-1} and $\sigma = 5.2$ cm^{-1}. For the intermediate frequencies, experiment, and theory are in good agreement. For lower and higher frequencies, the components deviate from the experiment. The maximum of the simulated spectrum is found for a diameter difference of about 0.66 nm, which is smaller than the experimental value of 0.72 nm reported in Refs. [46] and [49]. This shows, that the parameterizations of the LJ potential for graphite is not exact for the curved sp^2 networks of DWCNTs.

A progressive transition energy downshift for a given inner tube chirality for the split components with increasing Raman shifts is observed in Figure 8. Similarly to the frequency upshift, this can be understood by an increasing

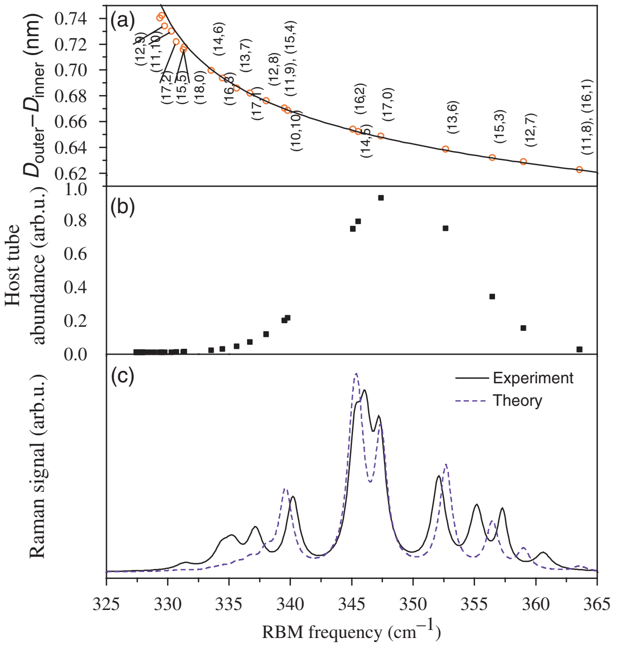

Fig. 9. (a) RBM frequency of a (6,4) inner tube as a function of the diameter difference to various outer tubes (indicated by their chiral vectors). (b) The abundance of the corresponding outer tubes used in the model calculation. (c) Raman line pattern for the RBM of the (6,4) inner tube as obtained from experiment (solid line) and from theory (dashed line) as described in the text. Reprinted with permission from [55] R. Pfeiffer et al. *Phys. Rev. B* 72, 161404 (**2005**). © 2005, American Physical Society.

interaction between the two shells for decreasing diameter difference. This interaction acts on the inner shell like a radial pressure. The pressure dependence of E_{22} for the (6,4) and the (6,5) inner tubes was calculated in Ref. [61] using an extended tight-binding method. The corresponding values are –7.8 meV/GPa and –2.5 meV/GPa. After Ref. [62], the frequencies shift with about 1.1 cm^{-1}/GPa. Thus one obtains –7.1 meV/cm^{-1} and –2.3 meV/cm^{-1}, respectively. The signs and the order of magnitude compare well with the experimental values. Additionally, one gets –3.6 meV/cm^{-1} from the measured pressure induced shift of the E_{22}^{S} transition[63] for a (6,5) tube of –4 meV/GPa, which is very close the experimental value of –2.7 meV/cm^{-1}.

In summary, the splitting of the inner tube modes to a large number of components as compared to the SWCNTs with the same chiralities is explained by the possibility of finding the same inner tube in a large number of outer ones with different diameters. The varying shell to shell distance for different inner-outer tube pairs for a fixed inner tube gives rise to significant shifts in the vibrational and transition energies, which can be quantitatively explained.

3.1.2. Phonon and Quasi-Particle Life-Times in DWCNTs

Now, we turn to discussion of the observed very narrow line-widths of the RBMs. This is the most important property of the inner tube RBMs, which will be exploited throughout in this work. Intrinsic line-widths can be determined by deconvoluting the experimental spectra with the spectrometer response fit a Voigtian fit, whose Gaussian component describes the spectrometer resolution and the Lorentzian gives the intrinsic line-width. The Lorentzian component for some inner tube RBMs is as small as 0.4 cm^{-1},[38] which is an order or magnitude smaller than the values obtained for isolated individual tubes in a normal SWCNT sample.[64] The narrow line-widths, i.e., long phonon life-times of the inner tube RBMs was originally associated to the perfectness of the inner tubes grown from the peapod templates.[38] It was found, however, that inner tubes in chemical vapor deposition (CVD) grown DWCNTs have similarly small line-widths.[44] In Figure 10, the high resolution spectra for the inner tube RBMs in CVD and peapod template grown DWCNTs is shown. This suggests, that the tube environment plays an important role in the magnitude of the observable RBM line-width.

The tube-tube interactions have been shown to give rise to up to ≈30 cm^{-1} extra shift to the RBMs.[55] The principal difference between SWCNTs and inner tubes in DWCNTs (irrespective whether these are CVD or peapod

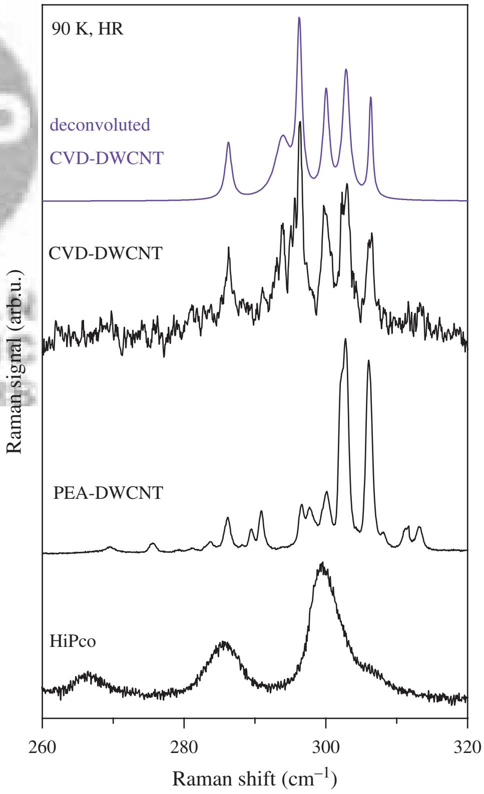

Fig. 10. High resolution Raman spectra taken at 676 nm laser excitation and 90 K on the CVD- and PEA-DWCNT and an SWCNT reference (HiPco) sample. The deconvoluted spectrum is also shown for the CVD-DWCNT sample. The narrow line-widths indicate the long RBM phonon life-times of the inner tubes in both DWCNT materials. Reprinted with permission from [44], F. Simon et al., *Chem. Phys. Lett.* 413, 506 (**2005**). © 2005, Elsevier.

template grown) is the different surrounding of a small diameter SWCNT with a given chirality: for the SWCNT sample, each tube is surrounded by the ensemble of other SWCNTs. For a close packed hexagonal bundle structure,[65] this involves 6 nearest neighbors with random chiralities. This causes an inhomogeneous broadening of the RBMs. However, the nearest-neighbor of an inner tube with a given chirality is an outer tube also with a well defined chirality. A given inner tube can be grown in several outer tubes with different diameters, however the chiralities of an inner-outer tube pair is always well defined, therefore the nearest neighbor interaction acting on an inner tube is also well-defined. As shown above, the interaction between most inner-outer tube pairs is strong enough to separate the inner tube RBMs from each-other thus giving rise to the well resolved split components of a given inner tube chirality.[58]

In addition to the long phonon life-times of inner tubes, the life-time of optical excitations, i.e., the life-time of the quasi-particle associated with the Raman scattering is unexpectedly long. To demonstrate this, we compare the resonant Raman scattering data for an inner tube and a SWCNT with the same chirality. In Figure 11 we show the energy profile of the resonant Raman scattering at some selected temperatures for two (6,4) tube modes: one is an inner tube in a DWCNT sample, the other is a SWCNT in a CoMoCat sample. Such energy profiles are obtained by taking an energy (vertical) cross section of a Raman map such as shown in Figure 8. The Raman intensities for a given excitation energy were obtained by fitting the spectra with Voigtian curves for the tube modes, whose Gaussian component accounts for the spectrometer resolution and whose Lorentzian for the intrinsic line-width. For the DWCNT sample, the strongest (6,4) inner tube component at 347 cm^{-1} and for the SWCNT CoMoCat sample the (6,4) tube mode at 337 cm^{-1} is shown. The temperature dependent resonant Raman data can be fitted with the conventional resonance Raman theory for Stokes Raman modes:[50, 66]

$$I(E_l) \propto \left| \frac{1}{(E_l - E_{ii} - i\Gamma)(E_l - E_{\mathrm{ph}} - E_{\mathrm{ii}} - i\Gamma)} \right|^2 \qquad (4)$$

Here, the electronic density of states is assumed to be a Dirac function, the matrix elements describing the electron-phonon interactions are assumed to be identical for a tube with the same chirality irrespective of the surrounding and temperature independent and are dropped from the equation, E_l is the exciting laser energy, E_{ii} is the transition energy, E_{ph} is the phonon energy and Γ is the damping parameter, i.e., the inverse of the quasi-particle life-time. The temperature dependence of the resonant Raman scattering is included in the T dependence of E_{ii} and Γ. For the (6,4) chirality, the E_{22} optical transition is observed.[55] The fitted curves are shown with solid lines in Figure 11.

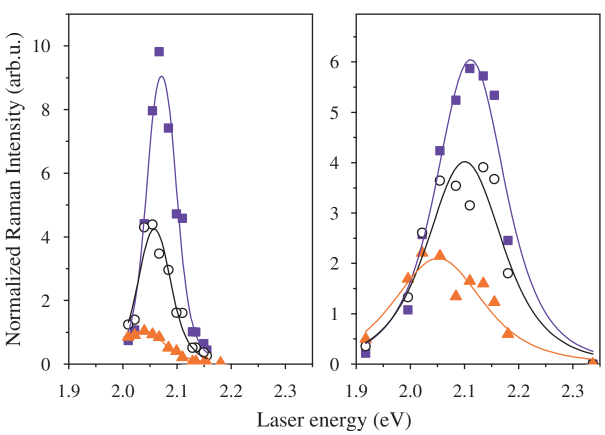

Fig. 11. Temperature dependent Raman resonance profile for the (6,4) tubes in the DWCNT and SWCNT (CoMoCat) samples, ■: 90 K, ○: 300 K, ▲: 600 K. For the DWCNT, the strongest, 347 cm^{-1} component is shown. Solid curves show fits with the resonant Raman theory as discussed in the text.

Clearly, the resonance width is always smaller for the DWCNT than for the SWCNT sample. In other words, the life-time of the optically excited quasi-particle is longer lived for the DWCNT. This explains why very strong inner tube modes are observed as the resonant Raman intensity is proportional to Γ^{-4}. The quasi-particle life-time is an important parameter for the application of carbon nanotubes in optoelectronic devices.[24, 25] As a result, DWCNTs appear to be superior in this respect than their one-walled counterparts.

3.1.3. Probing the SWCNT Diameter Distribution Through Inner Tube Growth

As discussed above, the Raman spectra of inner tubes have several advantages compared to that of the outer tubes: (i) their RBMs have a ~ factor 2 times larger splitting due to the smaller diameters, (ii) the line-widths are about 10 times narrower. The larger spectral splitting and narrower line-widths of the inner tube RBMs enable to characterize the inner tube diameter distribution with a spectral resolution that is about 20 times larger as compared to the analysis on the outer tubes. To prove that studying the inner tubes can be exploited for the study of outer ones, here we show that there is a one-to-one correspondence between the inner and outer tube diameter distributions following Ref. [49].

In Figure 12, we compare the inner tube RBM Raman spectra for four different DWCNT materials based on SWCNTs with different diameters and produced with different methods. The SWCNTs were two arc-discharge grown SWCNTs (SWCNT-N1 and N2) and two laser ablation grown tubes (SWCNT-R and SWCNT-L). The diameter distributions of the SWCNT materials were determined from Raman spectroscopy[66] giving $d_{\mathrm{N1}} = 1.50$ nm, $\sigma_{\mathrm{N1}} = 0.10$ nm, $d_{\mathrm{N2}} = 1.45$ nm, $\sigma_{\mathrm{N1}} = 0.10$ nm, $d_{\mathrm{R}} = 1.35$ nm,

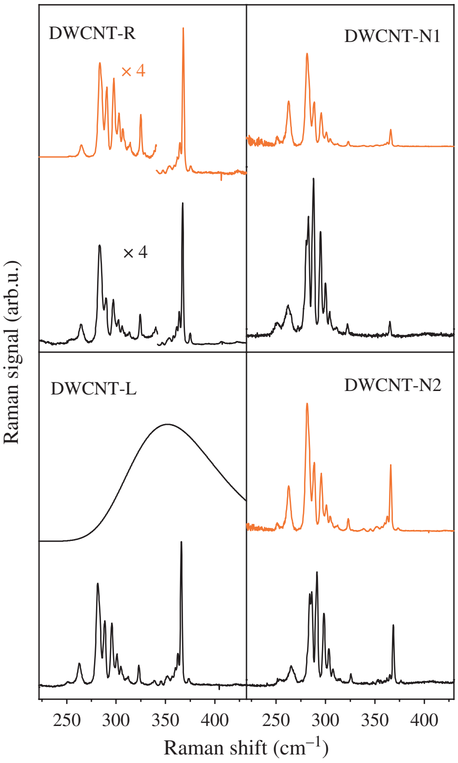

Fig. 12. As measured Raman spectra of the inner nanotube RBMs for four DWCNT samples (lower curves in each quarter) at 647 nm laser excitation. The upper spectra (shown in red) are smart scaled from the lower left spectrum. The Gaussian diameter distribution is shown for the DWCNT-L sample. Reprinted with permission from [49], F. Simon et al., *Phys. Rev. B* 71, 165439 (**2005**). © 2005, American Physical Society.

$\sigma_R = 0.09$ nm, and $d_L = 1.39$ nm, $\sigma_L = 0.09$ nm for the mean diameters and the variances of the distributions, respectively.

The spectra shown are excited with a 647 nm laser that is representative for excitations with other laser energies. The RBMs of all the observable inner tubes, including the split components,[38] can be found at the same position in all DWCNT samples within the ±0.5 cm^{-1} experimental precision of the measurement for the whole laser energy range studied. This proves that vibrational modes of DWCNT samples are robust against the starting material.

As the four samples have different diameter distributions, the overall Raman patterns look different. However, scaling the patterns with the ratio of the distribution functions (smart scaling) allows to generate the overall pattern for all systems, starting from e.g., DWCNT-L in the bottom-left corner of Figure 12. It was assumed that the inner tube diameter distributions follow a Gaussian function with a mean diameter 0.72 nm smaller than those of the outer tubes following Ref. [46] and with the same variance as the outer tubes. The empirical constants from Ref. [67] were used for the RBM mode Raman shift versus inner tube diameter expression. The corresponding Gaussian diameter distribution of inner tubes is shown for the DWCNT-L sample in Figure 12. A good agreement between the experimental and simulated patterns for the DWCNT-R sample is observed. A somewhat less accurate agreement is observed for the DWCNT-N1, N2 samples, which may be related to the different growth method: arc discharge for the latter, as compared to laser ablation for the R and L samples. The observed agreement has important consequences for the understanding of the inner tube properties. As a result of the photoselectivity of the Raman experiment, it proves that the electronic structure of the inner tubes is identical in the different starting SWCNT materials.

The scaling of the inner tube Raman spectra with the outer tube distribution shows that the inner tube abundance follows that of the outer ones. This agrees with the findings of X-ray diffractomery on DWCNTs[46] and is natural consequence of the growth of inner tubes inside the outer tube hosts. As a result, the inner-outer tube diameter distributions are similar to that shown schematically in Figure 13: the width of the inner outer tube distributions are the same, and the mean values differ by 0.72 nm. A cut-off in the inner tube diameter distribution was imposed at $d \approx 0.48$ nm due to the inability of C_{60} to enter into outer tubes smaller than 1.2 nm.[68–70]

In summary, the RBM frequencies of inner tubes with neighboring diameters are on the average four times more separated from each other than those of the outer ones.[67] In addition, the outer tube RBMs have a typical FWHM of 10 cm^{-1} (Ref. [64]) as compared to the FWHM of the inner tube RBMs of 0.4–0.5 cm^{-1}.[38] As a result, the available spectral resolution is at least 20 times larger when the RBMs of the inner tubes are investigated. This allows to

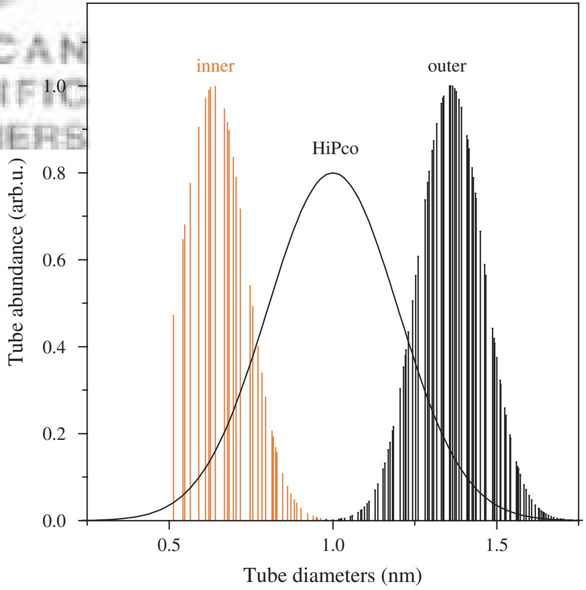

Fig. 13. Schematic diameter distribution of inner and outer tubes. Vertical lines denote a tube with a given chirality. Inner-outer tube relative abundances are not to scale. Note the inner tube abundance cut-off at ~0.5 nm. The diameter distribution for a HiPco SWCNT sample is shown for comparison.

study chirality or at least diameter selective reactions of the outer tubes by analyzing the inner tube response.

3.1.4. Studying the Reversible Hole Engineering Using DWCNTs

Soon after the discovery of the peapods,[31] it was recognized[33,71] that opening the SWCNTs by oxidation in air or by treating in acids is a prerequisite for good filling. Good filling means a macroscopic filling where the peapods are observable not only by local microscopic means such as HR-TEM but also by spectroscopy such as Raman scattering. On the other hand, a heat treatment around 1000 °C was known to close the openings which results in a low or no fullerene filling. It was also shown that the geometrically possible maximum of filling can be achieved when purified SWCNTs were subject to a 450 °C heat treatment in flowing oxygen.[72] However, these studies have concerned the overall fullerene filling, with no knowledge on the precise dependence on the thermal treatment or tube diameter specificity.

The high diameter and chirality sensitivity of Raman spectroscopy for the inner tubes allows to study the behavior of tube openings when subject to different treatments. More precisely, openings which allow fullerenes to enter the tubes can be studied. This is achieved by studying the resulting inner tube RBM pattern when the outer tube host was subject to some closing or opening treatments prior to the fullerene encapsulation.[73] Annealing of as purchased or opened tubes was performed at various temperatures between 800 °C and 1200 °C in a sealed and evacuated quartz tube at a rest gas pressure of 10^{-6} mbar. Opening of the tubes was performed by exposure to air at various temperatures between 350 °C and 500 °C.

Figure 14 shows the Raman response of tubes after the standardized DWCNT transformation conditions but different pre-treatment. Only the spectral range of the inner tube is shown in the main part of the figure. The spectrum at the center was recorded under identical conditions but the SWCNT was pre-annealed before the standardized filling and standardized transformation. Almost no response from inner shell tubes is observed for this material, which means no fullerenes had entered the tubes: the tubes were very efficiently closed by the annealing process. The small response just below 300 cm^{-1} could originate from some small leaks in the cage were a few C_{60} molecules or even more likely some carbon contamination had entered the primary tubes on a level which leads to less than 20% inner tubes for the larger diameter tubes and less than 3% for the smaller diameter tubes. The insert in Figure 14 depicts the RBM response from the outer tubes before and after annealing. The two spectra are almost identical, which proves that no outer tube coalescence had occurred at the temperature applied. The spectrum at the top in Figure 14 was recorded after reopening the annealed tubes at 500 °C on air and standard filling and transformation. The spectra derived from the pristine and from the reopened tubes are identical in all details. This means no dramatic damages by cutting a large number of holes into the sidewalls have happened. Consequently, the sidewalls of the tubes remain highly untouched by the opening process. Thus, it is suggested that fullerenes enter the tubes through holes at the tube ends.

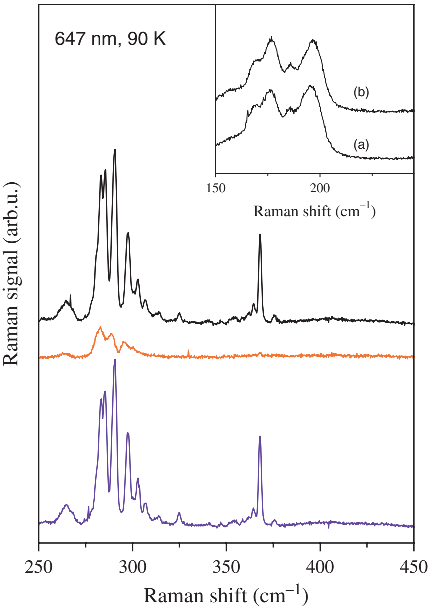

Fig. 14. Raman spectra in the spectral range of the inner shell tube RBM for nanotubes after special pre-treatment. Bottom: after filling as purchased tubes with C_{60} and standard transformation; Center: after annealing the as purchased tubes at 1000 °C for two hours, filling with C_{60} and standard transformation; Top: after re-opening the annealed samples, filling with C_{60}, and standard transformation. All spectra recorded at 90 K for 647 nm excitation and normalized to the response of the outer tube RBM of the pristine tubes. Insert: the RBM of the outer tubes before (a) and after (b) annealing at 1000 °C. Reprinted with permission from [73], F. Hasi et al., *J. Nanosci. Nanotechnol.* 5, 1785 (**2005**). © 2005, American Scientific Publishers.

The dependence of tube closing on annealing temperature and time was studied in more detail. Spectra for the RBM response were recorded for standard filling and standard transformation after various annealing temperatures and annealing times. The most important lines were evaluated with respect to their peak intensity. This intensity was related to the peak intensity of inner shell modes of DWCNTs grown from untreated starting material. This ratio is a quantitative measure for the fraction of tubes which remain open after the annealing procedure. I_0 and I_{annealed} are the intensity for the pristine and annealed tubes after standard filling and transformation, respectively. Results are depicted in Figure 15 for annealing at 800 °C (1073 K). A dramatic decrease of concentration for tubes remaining open after the annealing treatment is immediately recognized in Figure 15 with decreasing tube diameter (increasing RBM frequency). For tubes with 1.8 nm diameter (240 cm^{-1}) 98% remain open for a 20 min annealing at 800 °C whereas for the same annealing conditions

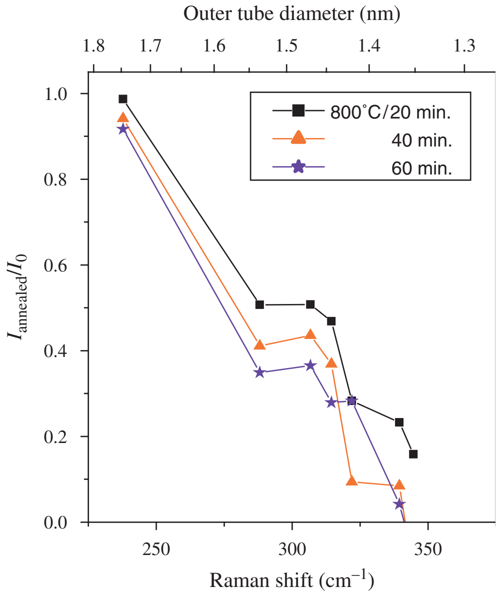

Fig. 15. Relative intensities, $I_{\mathrm{annealed}}/I_0$, of inner tube RBMs versus frequency (tube diameter) after various annealing conditions as indicated in the inserted legend. All spectra are normalized to the outer tube intensities. The upper scale shows the corresponding outer tube diameters. Reprinted with permission from [73], F. Hasi et al. *J. Nanosci. Nanotechnol.* 5, 1785 (**2005**). © 2005, American Scientific Publishers.

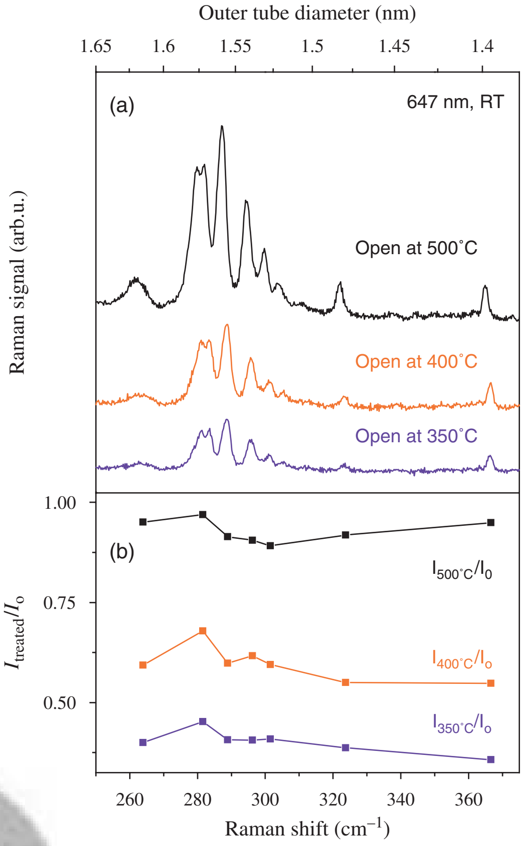

Fig. 16. Raman response of the RBM of inner shell CNTs for standard filling and transformation procedures after the pristine tubes had been closed and reopened at temperatures indicated (a). Part (b) depicts evaluated relative intensities versus Raman shift for the three different opening conditions. The upper scale provides outer tube diameters. Reprinted with permission from [73], F. Hasi et al., *J. Nanosci. Nanotechnol.* 5, 1785 (**2005**). © 2005, American Scientific Publishers.

and tubes with 1.3 nm diameter (345 cm^{-1}) only 15% remain open.

This technique can also be used to study the diameter selective tube opening process. Figure 16 depicts Raman spectra of the RBM recorded for 647 nm excitation for tubes which were closed at 1000 °C for two hours and then reopened by exposure to air at the temperatures indicated. As an overall result, the opening process becomes less and less efficient with decreasing temperature. However, the reduction in efficiency hardly depends on the tube diameter. The latter behavior is more evidently seen from an analysis of the response for the individual peaks as depicted in part (b) of Figure 16. For opening at 500 °C 95% of the closed tubes could be reopened, nominally independent of tube diameter. For opening at 400 °C only about 60% of the tubes could be opened. Surprisingly, as plotted this fraction is even slightly decreasing with decreasing tube diameter. Similarly, for opening at 350 °C only 45% of the tubes could be opened again, with a slight decrease of this fraction for small diameter tubes.

In summary, the reaction activity of holes in SWCNTs can be investigated by studying the process of filling the tubes with C_{60} fullerenes and transforming the latter to a set of small diameter inner tubes. Reversible closing and opening of the tubes can be achieved. The tube opening process is sensitive to temperature but insensitive to tube diameter. The almost identical Raman spectra for the pristine and for the opened tubes with respect to line positions, line-widths and line intensities suggest that the tube walls remain untouched and the holes for the tube filling are located at the tube ends. After tube closing, a small amount of inner tubes can be grown mostly in high defect areas of the tubes. In contrast to tube opening, the tube closing process is highly diameter sensitive.

3.2. Growth Mechanism of Inner Tubes Studied by Isotope Labeling

The growth of inner tubes from fullerenes raises the question, whether the fullerene geometry plays an important role in the inner tube growth or it acts as a carbon source only. Theoretical results suggest the earlier possibility.[74, 75] In addition, it needs clarification whether carbon exchange occurs between the two tube walls. Here, we review ^{13}C isotope labeled studies aimed at answering these two open questions. ^{13}C is a naturally occurring isotope of carbon with 1.1% abundance. In general, isotope substitution provides an important degree of freedom to study the effect of change in phonon energies while leaving the electronic properties unaffected. This have helped to unravel phenomena such as e.g., the phonon-mediated superconductivity.[76]

First, we discuss the inner tube growth from isotope labeled fullerenes,[51] and secondly we present the growth of inner tubes from isotope labeled organic solvents.[77]

Commercial ^{13}C isotope enriched fullerenes with two different enrichment grades were used to grow isotope enriched inner tubes. Fullerene encapsulation[33] and inner tube growth was performed with the conventional methods.[35] This results in a compelling isotope engineered system: double-wall carbon nanotubes with ^{13}C isotope enriched inner walls and outer walls containing natural carbon.[51]

In Figure 17(a), we show the inner tube RBM range Raman spectra for a natural DWCNT and two DWCNTs with differently enriched inner walls, 25% and 89%. These two latter samples are denoted as $^{13}C_{25}$- and $^{13}C_{89}$-DWCNT, respectively. The inner wall enrichment is taken from the nominal enrichment of the fullerenes used for the peapod production, whose value is slightly refined based on the Raman data. An overall downshift of the inner tube RBMs is observed for the ^{13}C enriched materials accompanied by a broadening of the lines. The downshift is clear evidence for the effective ^{13}C enrichment of inner tubes. The magnitude of the enrichment and the origin of the broadening are discussed below.

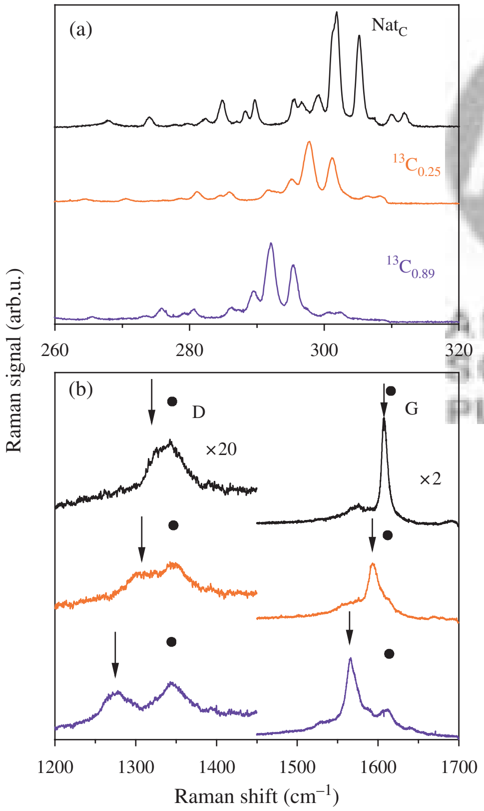

Fig. 17. Raman spectra of DWCNTs with natural carbon and ^{13}C enriched inner tubes at 676 nm laser excitation and 90 K. The inner tube RBM (a) and D and G mode spectral ranges (b) are shown. Arrows and filled circles indicate the D (left) and G (right) modes corresponding to the inner and outer tubes, respectively. Reprinted with permission from [51], F. Simon et al. *Phys. Rev. Lett.* 95, 017401 (**2005**). © 2005, American Physical Society.

The RBM lines are well separated for inner and outer tubes due to the $\nu_{RBM} \propto 1/d$ relation and a mean inner tube diameter of $d \sim 0.7$ nm.[46, 49] However, other vibrational modes such as the defect induced D and the tangential G modes strongly overlap for inner and outer tubes. Arrows in Figure 17(b) indicate a gradually downshifting component of the observed D and G modes. These components are assigned to the D and G modes of the inner tubes. The sharper appearance of the inner tube G mode, as compared to the response from the outer tubes, is related to the excitation of semiconducting inner tubes and metallic outer tubes.[38, 49]

The shifts for the RBM, D, and G modes can be analyzed for the two grades of enrichment. The average value of the relative shift for these modes was found to be $(\nu_0 - \nu)/\nu_0 = 0.0109(3)$ and 0.0322(3) for the $^{13}C_{0.25}$- and $^{13}C_{0.89}$-DWCNT samples, respectively. Here, ν_0 and ν are the Raman shifts of the same inner tube mode in the natural carbon and enriched materials, respectively. In the simplest continuum model, the shift originates from the increased mass of the inner tube walls. This gives $(\nu_0 - \nu)/\nu_0 = 1 - \sqrt{(12 + c_0)/(12 + c)}$, where c is the concentration of the ^{13}C enrichment on the inner tube, and $c_0 = 0.011$ is the natural abundance of ^{13}C in carbon. The resulting values of c are 0.277(7) and 0.824(8) for the 25 and 89% samples, respectively.

The growth of isotope labeled inner tubes allows to address whether carbon exchange between the two walls occurs during the inner tube growth. In Figure 18, we show the G′ spectral range for DWCNTs with natural carbon and ^{13}C enriched inner walls with 515 nm laser excitation. The G′ mode of DWCNTs is discussed in detail in Ref. [58] and it was introduced in Figure 5: the upper G′ mode component corresponds to the outer tubes and the lower to the inner tubes. The outer tube G′ components are unaffected by the ^{13}C enrichment within the 1 cm^{-1} experimental accuracy. This gives an upper limit to the extra ^{13}C in the outer wall of 1.4%. This proves that there is no sizeable carbon exchange between the two walls as this would result in a measurable ^{13}C content on the outer wall, too. This is important for the contrast of the NMR signal between the two walls as it is discussed further below: were the outer shell also enriched, one could not obtain a reliable information about the density of states on the inner shell alone.

The narrow RBMs of inner tubes and the freedom to control their isotope enrichment allows to precisely compare the isotope related phonon energy changes in the experiment and in *ab-initio* calculations. This was performed by Kürti and Zólyomi in Ref. [51]. The validity of the above simple continuum model for the RBM frequencies was verified by performing first principles calculations on the (n,m) = (5,5) tube as an example. In the calculation, the Hessian matrix was determined by DFT

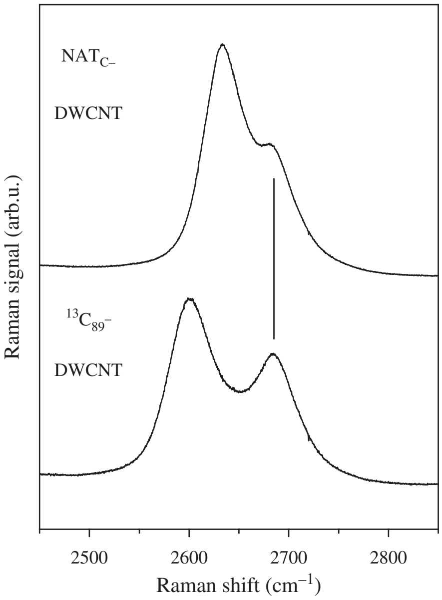

Fig. 18. G′ spectral range of DWCNTs with natural carbon and ^{13}C enriched inner walls with 515 nm laser excitation. Note the unchanged position of the outer tube G′ mode indicated by a vertical line.

using the Vienna *Ab Initio* Simulation Package.[78] Then, a large number of random ^{13}C distributions were generated and the RBM vibrational frequencies were determined from the diagonalization of the corresponding dynamical matrix for each individual distribution. The distribution of the resulting RBM frequencies can be approximated by a Gaussian where center and variance determine the isotope shifted RBM frequency and the spread in these frequencies. The difference between the shift determined from the continuum model and from the *ab-initio* calculations is below 1%.

The broadening for the ^{13}C enriched inner tubes is best observed for the narrow RBMs. In Figure 19(a–b) we show the RBMs of some inner tubes for the $^{\mathrm{Nat}}$C and $^{13}C_{0.25}$ samples. Curves (1) are the line-shapes after deconvolution with the Gaussian response of our spectrometer. In Figuer 19(a), the resulting line-shapes are Lorentzians, but in Figure 19(b), the line-shape still contains a Gaussian component, as discussed below. The FWHMs of the resulting line-shapes are 0.76(4), 0.76(4), 0.44(4), 0.54(4), and 1.28(6), 1.30(6), 1.12(6), 1.16(6) for the inner tube RBMs shown in Figure 19 of the $^{\mathrm{Nat}}$C and $^{13}C_{0.25}$ materials, respectively. The origin of the extra broadening is due to the random distribution of ^{12}C and ^{13}C nuclei. Calculations indicate that the ratio between the half width of extra broadening and the shift, $\Delta\nu/(\nu_0-\nu)$, is approximately 0.19 for a 30% ^{13}C enriched sample. The corresponding broadened line-shapes are shown in Figure 19(b) as curve (3). When the magnitude of the Gaussian randomness related broadening was fit (curve (2) in Fig. 19(b)), we found that $\Delta\nu/(\nu_0-\nu)=0.15$. Similar broadening was observed for the 89% sample which can also be reproduced by the calculation.

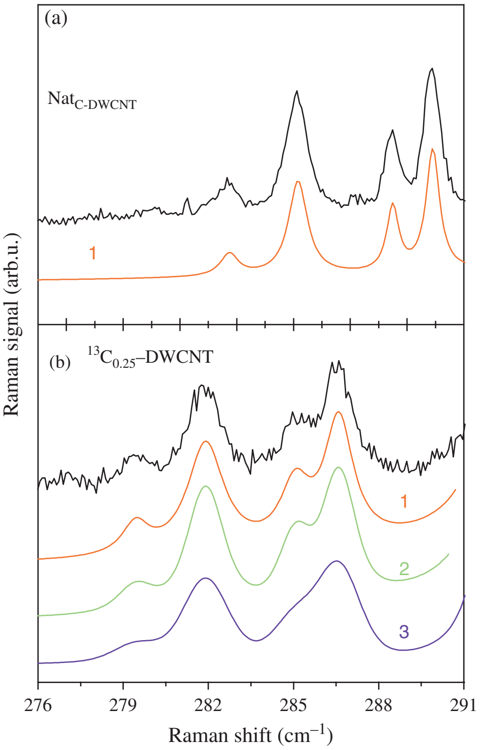

Fig. 19. RBMs of some inner tubes at 676 nm laser excitation with 0.5 cm^{-1} spectral resolution. (a) natural carbon-, (b) 25% ^{13}C enriched inner shell DWCNT. Curves are the line-shapes after deconvolution by the spectrometer response (1), the simulated line-shape with an extra Gaussian broadening to the intrinsic lines of the $^{\mathrm{Nat}}$C material (2), and the calculated line-shape (see text) (3). Reprinted with permission from [51], F. Simon et al. *Phys. Rev. Lett.* 95, 017401 (**2005**). © 2005, American Physical Society.

The known characteristics of isotope labeled inner tubes allow to study the possibility of inner tube growth from non-fullerene carbon sources.[77] For this purpose, we choose organic solvents containing aromatic rings, such as toluene and benzene. These are known to wet the carbon nanotubes and are appropriate solvents for fullerenes. As described in the following, the organic solvents indeed contribute to the inner tube growth, however only in the presence of C_{60} "stopper" molecules.[77] In the absence of co-encapsulated fullerenes the solvents alone give no inner tube.

The fullerene + organic solvents encapsulation was performed by dissolving typically 150 μg fullerenes in 100 μl solvents and then sonicating with 1 mg SWCNT in an Eppendorf tube for 1 h. The weight uptake of the SWCNT is ~15%[51] that is shared between the solvent and the fullerenes. The peapod material was separated from the solvent by centrifuging and it was then greased on a sapphire substrate. The solvent prepared peapods were treated in dynamic vacuum at 1250 °C for 2 hours for the inner tube growth. The inner tube growth efficiency was found independent of the speed of warming.

The growth of inner tubes from the solvents can be best proven by the use of C_{60} containing natural carbon and a solvent mixture consisting of ^{13}C enriched and natural carbon containing solvents with varying concentrations. Toluene was a mixture of ring ^{13}C labeled ($^{13}C_6H_6$–$^{NAT}CH_3$) and natural toluene ($^{NAT}C_7H_8$). Benzene was a mixture of ^{13}C enriched and natural benzene. The labeled site was >99% ^{13}C labeled for both types of molecules. The ^{13}C content, x, of the solvent mixtures was calculated from the concentration of the two types of solvents and by taking into account the presence of the naturally enriched methyl-group for the toluene. In Figure 20(a), we show the G′ modes of DWCNTs with varying ^{13}C labeled content in toluene + C_{60} based samples and in Figure 20(b), we show the same spectra after subtracting the outer SWCNT component. A shoulder appears for larger values of x on the low frequency side of the inner tube mode, whereas the outer tube mode is unchanged. Similar behavior was observed for the benzene + C_{60} based peapod samples (spectra not shown) although with a somewhat smaller spectral intensity of the shoulder. The appearance of this low frequency shoulder is evidence for the presence of a sizeable ^{13}C content in the inner tubes. This proves that the solvent indeed contributes to the inner tube formation as it is the only sizeable source of ^{13}C in the current samples. The appearance of the low frequency shoulder rather than the shift of the full mode indicates an inhomogeneous ^{13}C enrichment. A possible explanation is that smaller diameter nanotubes might be higher ^{13}C enriched as they retain the solvent better than larger tubes.

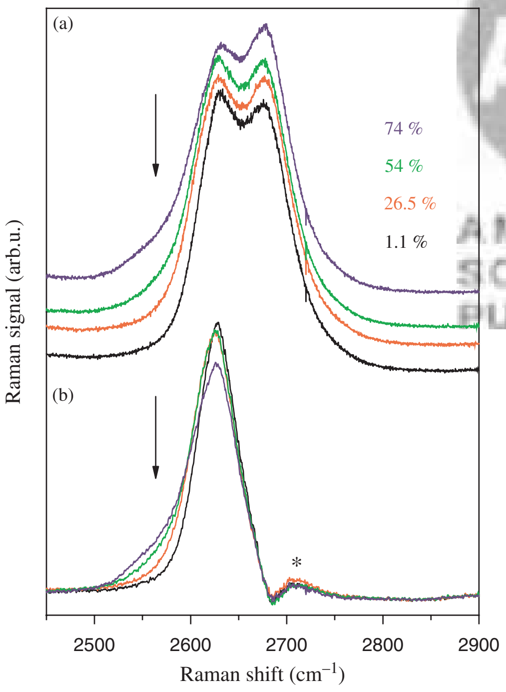

Fig. 20. (a) The G′ mode of toluene + C_{60} peapod based DWCNTs with varying ^{13}C enrichment at 515 nm laser excitation. From top to bottom: 74%, 54%, 26.5% and natural ^{13}C content. (b) The G′ mode of the inner tubes after subtracting the experimental SWCNT spectrum. A small residual peak is observed around 2710 cm^{-1} (denoted by an asterisk) due to the imperfect subtraction. Arrows indicate the spectral weight shifted toward lower frequencies. Reprinted with permission from [77], F. Simon and H. Kuzmany, *Chem. Phys. Lett.* 425, 85 (**2006**). © 2006, Elsevier.

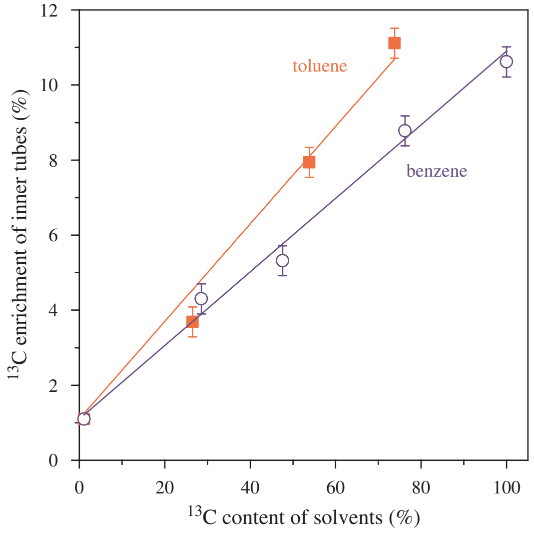

Fig. 21. ^{13}C content of inner tubes based on the first moment analysis as explained in the text as a function of ^{13}C enrichment of benzene and toluene. Lines are linear fits to the data and are explained in the text. Reprinted with permission from [77], F. Simon and H. Kuzmany, *Chem. Phys. Lett.* 425, 85 (**2006**). © 2006, Elsevier.

To quantify the ^{13}C enrichment of the inner tubes, the downshifted spectral weight of the inner tube G′ mode was determined from the subtracted spectra in Figure 21(b). The subtraction does not give a flat background above 2685 cm^{-1}, however it is the same for all samples and has a small spectral weight, thus it does not affect the current analysis. The line-shapes strongly deviate from an ideal Lorentzian profile. Therefore the line positions cannot be determined by fitting, whereas the first moments are well defined quantities. The effective ^{13}C enrichment of the inner tubes, c, is calculated from $(\nu_0 - \nu)/\nu_0 = 1 - \sqrt{(12 + c_0)/(12 + c)}$, where ν_0 and ν are the first moments of the inner tube G′ mode in the natural carbon and enriched materials, respectively, and $c_0 = 0.011$ is the natural abundance of ^{13}C in carbon. The validity of this "text-book formula" is discussed above and it was verified by *ab-initio* calculations for enriched inner tubes in Ref. [51]. In Figure 21, we show the effective ^{13}C content in the inner tubes as a function of the ^{13}C content in the starting solvents. The scaling of the ^{13}C content of the inner tubes with that in the starting solvents proves that the source of the ^{13}C is indeed the solvents. The highest value of the relative shift for the toluene based material, $(\nu_0 - \nu)/\nu_0 = 0.0041(2)$, corresponds to about 11 cm^{-1} shift in the first moment of the inner tube mode. The shift in the radial breathing mode range (around 300 cm^{-1})[56] would be only 1 cm^{-1}. This underlines why the high energy G′ mode is convenient for the observation of the moderate ^{13}C enrichment of the inner tubes. When fit with a linear curve with $c_0 + A * x$, the slope, A directly measures the carbon fraction in the inner tubes that originates from the solvents.

The synthesis of inner tubes from organic solvent proves that any form of carbon that is encapsulated inside SWCNTs contributes to the growth of inner tubes. As mentioned above, inner tubes are not formed in the absence of fullerenes but whether the fullerene is C_{60} or C_{70} does not play a role. It suggests that fullerenes act only as a stopper to prevent the solvent from evaporating before the synthesis of the inner tube takes place. It also clarifies that the geometry of fullerenes do not play a distinguished role in the inner tube synthesis as it was originally suggested.[74, 75] It also proves that inner tube growth can be achieved irrespective of the carbon source, which opens a new prospective to explore the in-the-tube chemistry with other organic materials.

3.3. NMR Studies on Isotope Engineered Heteronuclear Nanotubes

The growth of the "isotope engineered" nanotubes, i.e., DWCNTs with highly enriched inner wall allows to allows to study these samples with NMR with an unprecedented specificity for the small diameter carbon nanotubes. This allows a unique study of the electronic properties of such nanotubes. For normal SWCNTs, either grown from natural or ^{13}C enriched carbon, the NMR signal originates from all kinds of carbon like amorphous or graphitic carbon.

NMR allows to determine the macroscopic amount of enriched tubes in our sample as it is sensitive to the number of ^{13}C nuclei in the sample. In Figure 22, we show the static and magic angle spinning spectra of ^{13}C enriched DWCNTs, and the static spectrum for the SWCNT material. The mass fraction which belongs to the highly enriched phase can be calculated from the integrated signal intensity by comparing it to the signal intensity of the 89% ^{13}C enriched fullerene material. We found that the mass fraction of the highly enriched phase relative to the total sample mass is 13(4)%. The expected mass ratio of inner tubes as compared to the total sample mass is 15%, which is obtained from the SWCNT purity (50%), ~70% volume filling for peapod samples,[72] and the mass ratio of encapsulated fullerenes to the mass of the SWCNTs. Thus, the measured mass fraction of the highly enriched phase is very similar to that of the calculated mass fraction of inner tubes. This suggests that the NMR signal comes nominally from the inner tubes, and other carbon phases such as amorphous or graphitic carbon are non ^{13}C enriched.

The typical chemical shift anisotropy (CSA) powder pattern is observed for the SWCNT sample in agreement with previous reports.[79, 80] However, the static DWCNT spectrum cannot be explained with a simple CSA powder pattern even if the spectrum is dominated by the inner tube signal. The complicated structure of the spectrum suggests that the chemical shift tensor parameters are highly distributed for the inner tubes. It is the result of the higher curvature of inner tubes as compared to the outer ones: the variance of the diameter distribution is the same for the inner and outer tubes[81] but the corresponding bonding angles show a larger variation.[82] In addition, the residual line-width in the MAS experiment, which is a measure of the sample inhomogeneity, is 60(3) ppm, i.e., about twice as large as the ~35 ppm found previously for SWCNT samples.[79, 80] The isotropic line position, determined from the MAS measurement, is 111(2) ppm. This value is significantly smaller than the isotropic shift of the SWCNT samples of 125 ppm.[79, 80] However, recent theoretical *ab-initio* calculations have successfully explained this anomalous isotropic chemical shift.[83] It was found that diamagnetic demagnetizing currents on the outer walls cause the diamagnetic shift of the inner tube NMR signal.

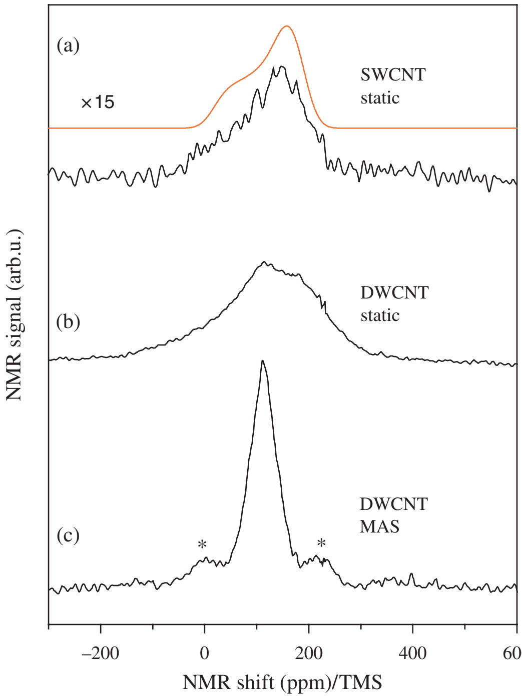

Fig. 22. NMR spectra normalized by the total sample mass, taken with respect to the tetramethylsilane (TMS) shift. (a) Static spectrum for non-enriched SWCNT enlarged by 15. Smooth solid line is a chemical shift anisotropy powder pattern simulation with parameters published in the literature [79]. (b) Static and (c) MAS spectra of $^{13}C_{0.89}$-DWCNT, respectively. Asterisks show the sidebands at the 8 kHz spinning frequency. Reprinted with permission from [51], F. Simon et al., *Phys. Rev. Lett.* 95, 017401 (**2005**). © 2005, American Physical Society.

In addition to the measurement of the line position, the dynamics of the nuclear relaxation is a sensitive probe of the local electronic properties.[85] The electronic properties of the nanotubes was probed using the spin lattice relaxation time, T_1, defined as the characteristic time it takes the ^{13}C nuclear magnetization to recover after saturation.[84] The signal intensity after saturation, $S(t)$, was deduced by integrating the fast Fourier transform of half the spin-echo for different delay times t. The data were taken with excitation pulse lengths $\pi/2 = 3.0$ μs and short pulse separation times of $\tau = 15$ μs.[85] The value of T_1 was obtained by fitting the t dependence of $S(t)$ to the form

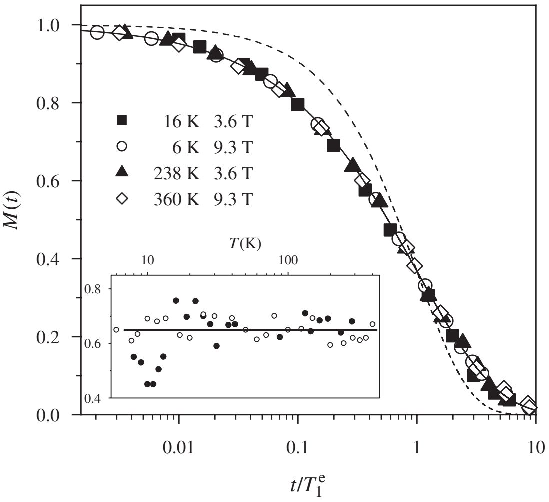

Fig. 23. Reduced nuclear magnetization recovery, $M(t)$, as a function of the scaled delay time t/T_1^e (see Eq. (5)), for various temperature and magnetic field values. Both axes are dimensionless. Solid curve shows stretched exponential fit with $\beta = 0.65$ and dashed curve shows single exponential with $\beta = 1$. Inset shows temperature dependence of the best fit values of β at 3.6 Tesla (●) and 9.3 Tesla (○), and average value of the data set $\beta = 0.65$ (solid line). Reprinted with permission from [84], P. M. Singer et al., *Phys. Rev. Lett.* 95, 236403 (**2005**). © 2005, American Physical Society.

$S(t) = S_a - S_b \cdot M(t)$, where $S_a \simeq S_b$ (>0) are arbitrary signal amplitudes, and

$$M(t) = \exp[-(t/T_1^e)^\beta] \tag{5}$$

is the reduced magnetization recovery of the ^{13}C nuclear spins. Figure 23 shows the results of $M(t)$ for the inner-tubes as a function of the scaled delay time t/T_1^e, under various experimental conditions listed in the Figure. We find that $M(t)$ does not follow the single exponential form with $\beta = 1$ (dashed line), but instead fits well to a stretched exponential form with $\beta \simeq 0.65(5)$, implying a distribution in the relaxation times T_1. The data in Figure 23 is displayed on a semi-log scale for the time axis in order to emphasize the data for earlier decay times and to illustrate the collapse of the data set for the upper 90% of the NMR signal. For a broad range of experimental conditions, the upper 90% of the $M(t)$ data is consistent with constant $\beta \simeq 0.65(5)$ (see inset), implying a field and temperature independent underlying distribution in T_1. The lower 10% of the $M(t)$ data, corresponding to longer delay times, comes from the non-enriched outer-walls which have much longer relaxation times under similar experimental conditions.[79, 80]

The collapse of the data set in Figure 23 to Eq. (5) with constant $\beta = 0.65(5)$ is a remarkable experimental observation. From an experimental point of view, it implies that all one needs in order to characterize the T and H dependence of the underlying T_1 distribution is the bulk (or average) value, T_1^e (Eq. (5)). From an interpretational point of view, it implies that each inner-tube in the powder sample has a different value of T_1, yet *all* the T_1 components and therefore all the inner-tubes follow the same T and H dependence within experimental uncertainty. This finding is in contrast to earlier reports in SWCNTs where $M(t)$ fits well to a bi-exponential distribution, 1/3 of which had a short T_1 value characteristic of fast relaxation from metallic tubes, and the remaining 2/3 had long T_1 corresponding to the semiconducting tubes,[79, 80, 86, 87] as expected from a macroscopic sample of SWCNTs with random chiralities. The data for the inner-tubes in DWCNTs differ in that a similar bi-exponential fit to $M(t)$ is inconsistent with the shape of the recovery in Figure 23. Furthermore, if there were 1/3 metallic and 2/3 truly semi-conducting inner-tubes in the DWCNT sample, one would expect the ratio of T_1 between semiconducting and metallic tubes to increase exponentially with decreasing T below the semiconducting gap (~5000 K), and therefore one would expect an increasingly large change in the underlying distribution in T_1 with decreasing T. This change would manifest itself as a large change in the shape of the $M(t)$, however this is not the case as shown in Figure 23. The possibility of two components in T_1 with different T dependence can therefore be ruled out, and instead it could be concluded that all T_1 components (corresponding to distinct inner-tubes) exhibit the same T and H dependence within experimental scattering.

The experimentally observed uniform metallicity of inner tubes is a surprising observation. This is suggested to be caused by the shifting of the inner tube Fermi levels due to charge transfer between the two tube walls. Indeed, using *ab-initio* calculations Okada and Oshiyama have found that DWCNTs made of non-metallic zig-zag inner-outer tubes, such as the (7,0)@(16,0) DWCNT, are metallic.[88] The direction of the charge transfer goes against the Faraday effect as inner tubes are electron and outer tubes are hole doped. Although, calculations are difficult if not impossible for an arbitrary inner-outer tube pair, this result confirms that two non-metallic tubes when producing an inner tube can render the electronic structure metallic.

With these arguments, the bulk average T_1^e defined in Eq. (5) can be considered and its uniform T and H dependence can be followed. The $M(t)$ data can be fitted with the constant exponent $\beta = 0.65(5)$, which reduces unnecessary experimental scattering in T_1^e. In Figure 24 we show the temperature dependence of $1/T_1^eT$ in for two different values of the external magnetic field H. The data can be separated into two temperature regimes; the high temperature regime $\gtrsim$150 K, and the low T regime $\lesssim$150 K. At high temperatures, $1/T_1^eT$ is independent of T which indicates a metallic state[85] for all of the inner tubes. A strong magnetic field dependence for T_1 was also observed, which was explained by a 1D spin diffusion mechanism for T_1.[84]

The origin of the unusual T dependence of $1/T_1^eT$ in the low temperature regime ($\lesssim$150 K) is very peculiar.

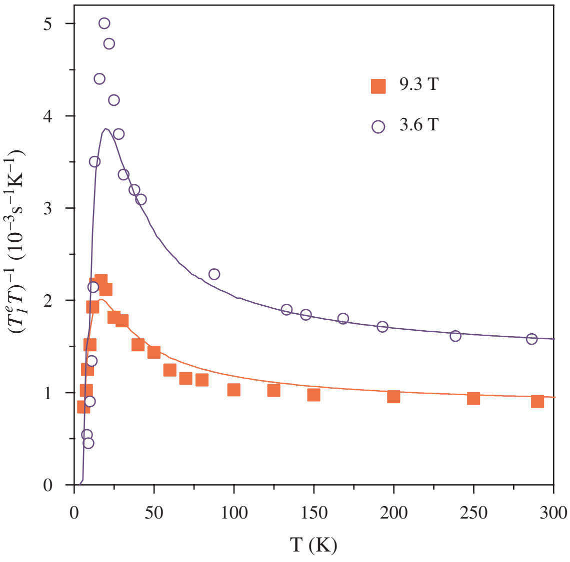

Fig. 24. Temperature dependence of spin-lattice relaxation rate divided by temperature, $1/T_1^eT$, in units of ($10^3\times$s^{-1}K^{-1}). Grey curves are best fits to Eq. (7) with $2\Delta = 46.8(40.2)$ K for $H = 3.6(9.3)$ Tesla, respectively. Reprinted with permission from [84], P. M. Singer et al., *Phys. Rev. Lett.* 95, 236403 (**2005**). © 2005, American Physical Society.

Some trivial explanations can be ruled out as its origin. Firstly, one can rule out the possibility of an activation type mechanism where T_1 is dominated by fluctuating hyperfine fields with a characteristic time scale τ which increases with decreasing T (i.e., glassy slowing). This would result in a peaked relaxation with a strongly field dependent peak value,[85] which is clearly not the case. Furthermore at low T, $1/T_1^eT$ drops below its high temperature value, which rules out the possibility of a T independent component in $1/T_1^eT$ plus an activated component on top. Secondly, the possibility of a simple $1/T$ Curie-like T dependence in $1/T_1^eT$ as a result of paramagnetic centers in the sample can be ruled out. This can be inferred from the pronounced gap in $1/T_1^eT$, together with the fact that no loss of ^{13}C NMR signal intensity in the entire temperature range of the experiment was observed. This implies that all the ^{13}C nuclei measure a gap in the spin excitation spectrum which cannot be explained by a Curie-like mechanism.

Following these considerations, one is lead to consider the simplest possible explanation for the experimental data in a non-interacting electron model of a 1D semiconductor with a small secondary gap (SG). The SG may be a result of the finite inner-wall curvature.[9, 89, 90, 47] The $1/T_1^eT$ data can be fitted using this non-interacting model with only one free parameter, the homogeneous SG, 2Δ. The normalized form of the gapped 1D density-of-states $n(E)$

$$n(E) = \begin{cases} \dfrac{E}{\sqrt{E^2-\Delta^2}} & \text{for } |E| > \Delta \\ 0 & \text{otherwise} \end{cases} \qquad (6)$$

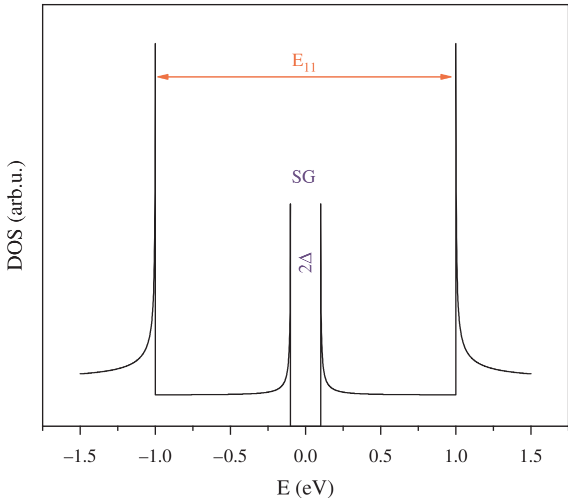

Fig. 25. Schematics of the density of states proposed to explain the relaxation results. A small energy, 2Δ a few meV secondary gap opens at the Fermi level of metallic inner tubes, which is displayed not to scale. Note the van Hove singularities (vHs) at $\pm\Delta$. The unaffected vHs of the original band structure are shown for the first optical transition (E_{11}).

here, E is taken with respect to the Fermi energy). The total DOS of an inner tube is shown schematically in Figure 25. Eq. (7) is used to calculate $1/T_1^eT$[91] as such

$$\frac{1}{T_1^eT} = \alpha(\omega)\int_{-\infty}^{\infty} n(E)n(E+\omega)\left(-\frac{\delta f}{\delta E}\right)dE \qquad (7)$$

where E and ω are in temperature units for clarity, f is the Fermi function $f = [\exp(E/T)+1]^{-1}$, and the amplitude factor $\alpha(\omega)$ is the high temperature value for $1/T_1^eT$. The results of the best fit of the data to Eq. (7) are presented in Figure 24, where $2\Delta = 43(3)$ K ($\equiv$3.7 meV) is H independent within experimental scattering between 9.3 and 3.6 Tesla. We note that at the largest external field of 9.3 Tesla, $\omega = 4.5$ mK $\ll \Delta, T$, however, ω must be retained inside the integral. This is a direct consequence of the one dimensionality which gives a logarithmic divergence inside the integral (solved numerically) of the form $\ln(T/\omega)$ for $T \lesssim \Delta$. At the lowest temperatures $T (\lesssim 5$ K), T_1^e ($\gtrsim$300 s) becomes so long that the low energy excitations specific to the homogeneous properties of the inner-tubes become inefficient, and other excitations take over, possibly defect related. In such cases we find that the recovery shape is no longer universal and the underlying distribution in T_1 is smoothed out, possibly due to spin-diffusion effects.

The origin of the experimentally observed gap still remains to be clarified. Tight binding calculations predict that applied magnetic fields can induce SG's of similar magnitude for metallic SWCNT.[92] However, such a scenario can be excluded due to the absence of any field dependence of the gap. The NMR data would be more consistent with a curvature induced SG for metallic tubes,[9, 89, 90, 47] however for the typical inner-tubes the predicted values, ~100 meV, are over an order of magnitude larger than our experimental data. Other scenarios, such as quantization of levels due to finite short lengths of the nanotubes could be considered as well, however, in all these cases a behavior independent of tube size and chirality is certainly not expected.

This suggests that electron–electron interactions play an important role for the metallic inner tubes. It has been predicted that electron–electron correlations and a Tomonaga-Luttinger (TLL) state leads to an increase in $1/T_1T$ with decreasing T,[93] which is a direct consequence of the 1D electronic state. The correlated 1D nature may also lead to a Peierls instability[10] with the opening of a small collective gap 2Δ and a sharp drop in $1/T_1T$ below $\Delta \sim 20$ K. Therefore, the presence of both a TLL state and a Peierls instability could possibly account for the data.

Summarizing the NMR studies on DWCNTs, it was shown that T_1 has a similar T and H dependence for all the inner-tubes have, with no indication of a metallic/semiconducting separation due to chirality distributions. At high temperatures ($T \gtrsim 150$ K) $1/T_1^eT$ of the inner tubes exhibit a metallic 1D spin diffusion state. Below ~150 K, $1/T_1^eT$ increases dramatically with decreasing T, and a gap in the spin excitation spectrum is found below $\Delta \simeq 20$ K. A 1D correlated state was suggested to be responsible for the opening of a small collective gap in the excitations, possibly a Peierls instability.[10, 56] Certainly, theoretical work on the electronic properties of inner wall nanotubes in DWCNT, and on the incidence of 1D correlation effects are needed to clarify the exact nature of the ground states.

3.4. ESR Studies on Encapsulated Magnetic Fullerenes

Observation of the intrinsic ESR signal of pristine SWCNTs remains elusive.[94, 95] Now, it is generally believed that intrinsic ESR of the tubes can not be observed as conduction electrons on metallic tubes are relaxed by defects too fast to be observable. In addition, one always observes a number of ESR active species in a sample, such as graphitic carbon or magnetic catalyst particles, which prevent a meaningful analysis of the signal. In contrast, local probe studies could still allow an ESR study of tubes, provided the local spin probe can be selectively attached to the tubes. This goal can be achieved by using magnetic fullerenes, such as e.g., N@C_{60} or C_{59}N, since fullerenes are known to be selectively encapsulated inside SWCNTs[31] and can be washed from the outside using organic solvents.[33] As the properties and handling of the two magnetic fullerenes are quite different, the synthesis of the corresponding peapods and the results are discussed separately.

N@C_{60} is an air stable fullerene[96] but decays rapidly above ~200 °C[97] which prevents the use of the conventional vapor method of peapod preparation which requires temperatures above 400 °C. To overcome this limitation and to allow in general the synthesis of temperature sensitive peapod materials, low temperature peapod synthesis (solvent method) was developed independently by four groups.[39–42] These methods share the common idea of mixing the opened SWCNTs with C_{60} in a solvent with low fullerene solubility such as methanol[39] or n-pentane.[40] The encapsulation is efficient as it is energetically preferred for C_{60} to enter the tubes rather than staying in the solution. After the solvent filling, excess fullerenes can be removed by sonication in toluene, which is a good fullerene solvent as it was found that fullerenes enter the tube irreversibly. HR-TEM has shown an abundant filling with the fullerenes[39, 41] but here we discuss macroscopic characterizations using Raman spectroscopy, which has proven that peapods prepared by the solvent method are equivalent to the vapor prepared peapods.

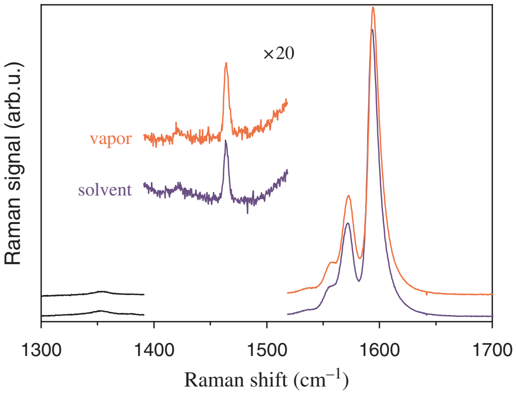

Fig. 26. Raman spectra of vapor and solvent filled C_{60}@SWCNT at 488 nm excitation and 90 K. The spectra are normalized to the amplitude of the SWCNT G mode. Reprinted with permission from [40], F. Simon et al., *Chem. Phys. Lett.* 383, 362 (**2004**). © 2004, Elsevier.

In Figure 26, we show the comparison of the Raman spectra of vapor- and solvent-filled C_{60} peapod samples. The Raman spectra of peapod samples in the plotted frequency range consist of the SWCNT G and D modes at 1590 and 1355 cm^{-1}, respectively and narrow lines related to the Raman active modes of the C_{60} inside the SWCNT.[33, 43] We show enlarged the most significant Raman active line of C_{60} peapod, the $A_g(2)$ mode. We observe a single $A_g(2)$ line at 1466 cm^{-1} for both peapod materials which is consistent with the relatively large, $d =$ 1.4 nm, tube diameter.[54] The observation of the 1466 cm^{-1} C_{60} $A_g(2)$ mode is characteristic[43] for the encapsulated C_{60}. Its observation for the solvent prepared sample with the same intensity as for the vapor prepared sample proves the effective macroscopic filling. The absence of an extra line at 1469 cm^{-1}, that is the Raman shift of the $A_g(2)$ of crystalline C_{60} is evidence that no C_{60} is present apart from those encapsulated in the nanotubes.

The low temperature synthesis allows to encapsulate the N@C_{60} fullerene. The N@C_{60} : C_{60} endohedral fullerene: fullerene solid solution can be produced in a N_2 arc-discharge tube following Ref. [98] with a typical yield of a few 10 ppm.[99] In Figure 27, the ESR spectra of the starting SWCNT, (N@C_{60} : C_{60})@SWCNT, and N@C_{60} : C_{60} are shown. The ESR spectrum of the pristine SWCNT for

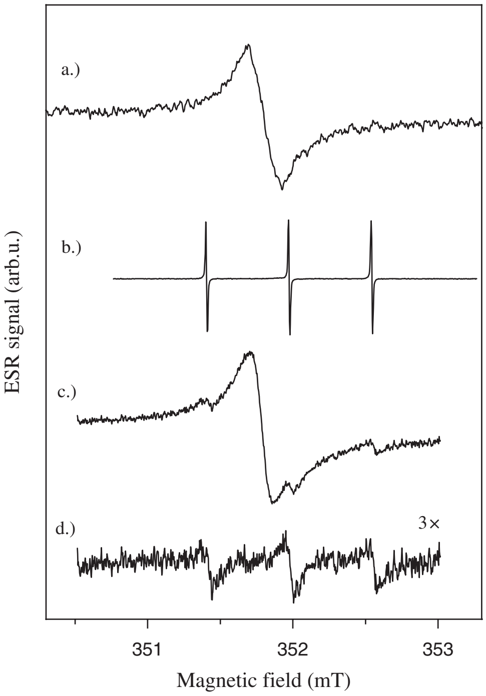

Fig. 27. X-band electron spin resonance spectrum of the (a) pristine SWCNT, (b) crystalline $N@C_{60}:C_{60}$, (c) $(N@C_{60}:C_{60})$@SWCNT, and (d) the triplet component of the $(N@C_{60}:C_{60})$@SWCNT ESR spectrum at ambient temperature. Reprinted with permission from [40], F. Simon et al., *Chem. Phys. Lett.* 383, 362 (**2004**). © 2004, Elsevier.

the magnetic field range shown is dominated by a signal that is assigned to some residual carbonaceous material, probably graphite. Figure 27(c). shows, that after the solvent encapsulation of $N@C_{60}:C_{60}$ in the NCL-SWCNT, a hyperfine N triplet ESR is observed, similar to that in pristine $N@C_{60}:C_{60}$, superimposed on the broad signal present in the pristine nanotube material. Figure 27(d) shows the triplet component of this signal after subtracting the signal observed in pristine SWCNT. The hyperfine triplet in $N@C_{60}:C_{60}$ is the result of the overlap of the $^4S_{3/2}$ state of the three 2p electrons of the N atom and the ^{14}N nucleus, with nuclear spin, $I = 1$. The isotropic hyperfine coupling of $N@C_{60}:C_{60}$ is unusually high as a result of the strongly compressed N atomic $2p^3$ orbitals in the C_{60} cage thus it unambiguously identifies this material.[96] The hyperfine coupling constant observed for the triplet structure in the encapsulated material, $A = 0.57 \pm 0.01$ mT, agrees within experimental precision with that observed in $N@C_{60}:C_{60}$,[96] which proves that the encapsulated material is $(N@C_{60}:C_{60})$@SWCNT. The ESR line-width for the encapsulated material, $\Delta H_{pp} = 0.07$ mT, is significantly larger than the resolution limited $\Delta H_{pp} = 0.01$ mT in the pristine $N@C_{60}:C_{60}$ material, the lines being Lorentzian. The most probable cause for the broadening is static magnetic fields from residual magnetic impurities in the SWCNT.[79] The ESR signal intensity is proportional to the number of N spins, and this allows the quantitative comparison of N concentrations in $(N@C_{60}:C_{60})$@SWCNT and $N@C_{60}:C_{60}$. Taking the filling value from the EELS measurement, we obtain that the N spin concentration in $(N@C_{60}:C_{60})$@SWCNT is ~2.5 times smaller than in the starting $N@C_{60}:C_{60}$ material. This cannot be due to a loss of N spins during the synthesis as $N@C_{60}:C_{60}$ is stable below 100 °C and N loss becomes rapid above 220 °C only.[97] However, the observed difference may be caused by the limited accuracy of the ESR intensity measurement also caused by microwave losses as the conducting buckypaper pieces are separated from each-other in a poorly controlled way.

As seen from the ESR results on encapsulated $N@C_{60}$, relatively limited information can be deduced about the tubes themselves. This stems from the fact that the N spins are well shielded in $N@C_{60}$[100] and are thus are relatively insensitive to the SWCNT properties. In contrast, $N@C_{60}$@SWCNT peapods might find another application as building elements of a quantum computer as proposed by Harneit et al.[8] A better candidate for magnetic fullerene encapsulation is the $C_{59}N$ monomer radical as here the unpaired electron is on the cage and is a sensitive probe of the environment. This material can be chemically prepared,[101] however it forms a non-magnetic dimer crystal $(C_{59}N)_2$. It appears as a spinless monomer in an adduct form[102] or attached to surface dangling bonds.[103] The magnetic $C_{59}N$ monomer radical is air sensitive but it can be stabilized as a radical when it is dilutely mixed in C_{60}.[104] As a result, a different strategy has to be followed to encapsulate $C_{59}N$ inside SWCNT, which is discussed in the following along with preliminary ESR results.[105]

To obtain $C_{59}N$ peapods, air stable $C_{59}N$ derivatives, ($C_{59}N$-der in the following) were prepared chemically by A. Hirsch and F. Hauke following standard synthesis routes.[102, 106] The $C_{59}N$-der was 4-Hydroxy-3,5-dimethyl-phenyl-hydroazafullerene whose structure is shown in Figure (28). The $C_{59}N$ derivatives were encapsulated either pure or mixed with C_{60} as $C_{59}N\text{-der}:C_{60}$ with 1 : 9 concentrations using a modified version of the low temperature encapsulation method. In brief, the mixture of the dissolved fullerenes and SWCNTs were sonicated in toluene

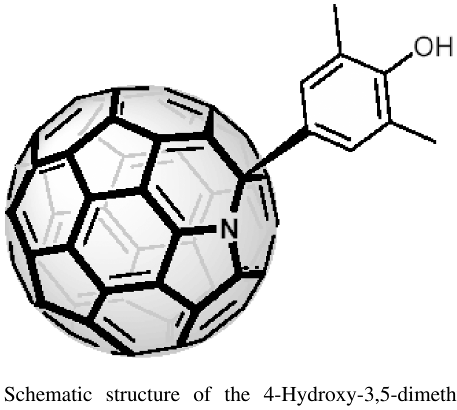

Fig. 28. Schematic structure of the 4-Hydroxy-3,5-dimethyl-phenyl-hydroazafullerene. Reprinted with permission from [105], F. Simon et al. *Carbon* 44, 1958 (**2006**). © 2006, Elsevier.

and filtered. It is expected that the $C_{59}N$ monomer radical can be obtained after a heat treatment in dynamic vacuum, which is discussed below.

Raman spectroscopy was performed to characterize the SWCNT filling with the $C_{59}N$-der. In Figure 29, the Raman spectra of the pristine and encapsulated $C_{59}N$-der is shown. The Raman spectra of the peapod sample (lower curve in Fig. 29) in the plotted frequency range consist of the SWCNT G modes around 1550 cm^{-1} and additional lines related to the Raman active modes of the encapsulated azafullerene derivative.[43] The major Raman modes of the pristine $C_{59}N$-der are similar to those of the $(C_{59}N)_2$ dimer.[107] The strongest mode is observed at 1459.2 cm^{-1} which is derived from the C_{60} $A_g(2)$ mode and is downshifted to 1457 cm^{-1} after the encapsulation procedure. The 2.2 cm^{-1} downshift proves the encapsulation of the molecule inside the SWCNT. When encapsulated inside SWCNTs, the corresponding $A_g(2)$ mode of C_{60} downshifts with 3 cm^{-1}, which is assigned to the softening of the C_{60} $A_g(2)$ vibrational mode due to the interaction between the ball and the SWCNT wall.[43] The slight difference between the downshift for the azafullerene and for the C_{60} peapods might be attributed to the different structure of the two molecules. The encapsulation also manifests in a line broadening: the main component of the 1457 cm^{-1} mode is broadened from 4.5 cm^{-1} FWHM in the pristine material to 10 cm^{-1} FWHM in the encapsulated one. This is similar to the values found for encapsulated C_{60}.[43]

The integrated intensity of the observed $A_g(2)$ derived mode of the $C_{59}N$ is approximately 5 times larger than that of a C_{60} peapod prepared identically when normalized by the SWCNT G mode intensity. This, however, can not be used to measure the encapsulation efficiency as Raman intensities depend on the strength of the Raman resonance enhancement and the Raman scattering matrix elements.[50] For C_{60} peapods the Raman signal was calibrated with independent and carbon number sensitive measurements: EELS studies gave the total number of C_{60} related and non-C_{60} related carbons[72] and the mass of encapsulated C_{60}s was determined from NMR studies using ^{13}C enriched fullerenes.[51, 84] In the current case, neither methods can be employed and we determined the filling efficiency for the azafullerene by encapsulating a mixture of the azafullerene and C_{60}. In Figure 30, the Raman spectra of the encapsulated $C_{59}N$-der : C_{60} mixture with weight ratios of 1 : 9 in the starting solvent is shown. The Raman spectrum of the encapsulated mixture was simulated with a weighted sum of the separately recorded

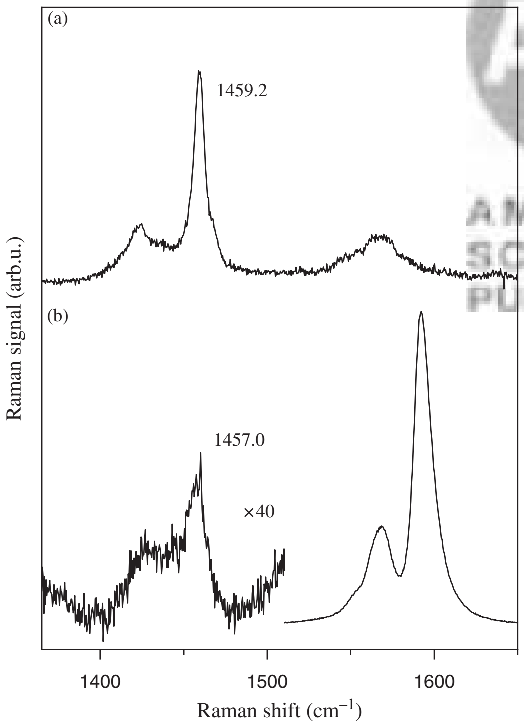

Fig. 29. Tangential mode of the Raman spectra of the $C_{59}N$-der before (a) and after encapsulation (b) excited with a 488 nm laser. Labels mark the position of the strongest $C_{59}N$-der mode in the two samples. The Raman G-mode of SWCNT dominates the peapod spectrum in the 1550–1650 cm^{-1} range. Reprinted with permission from [105], F. Simon et al., *Carbon* 44, 1958 (**2006**). © 2006, Elsevier.

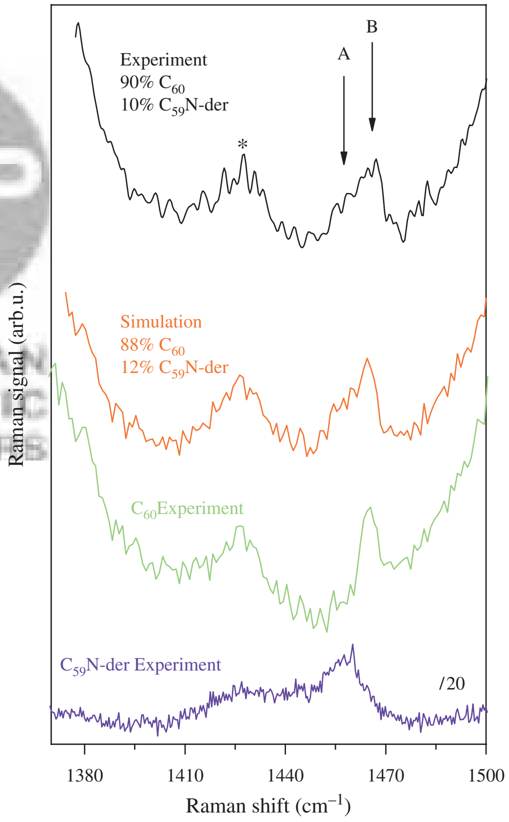

Fig. 30. Raman spectra of the encapsulated $C_{59}N$-der : C_{60} mixture at the 488 nm laser excitation. The spectra for the $C_{59}N$-der and C_{60} peapods is shown together with their weighted sum as explained in the text. A and B mark the components coming nominally from the superposing two phases. The asterisk marks a mode that is present in the pristine SWCNT material. Note the different scale for the $C_{59}N$-der peapod material. Reprinted with permission from [105], F. Simon et al., *Carbon* 44, 1958 (**2006**). © 2006, Elsevier.

spectra for encapsulated C_{59}N-der and C_{60}. The best agreement between the simulated and the experimental spectra is for a C_{59}N-der content of 0.12(2). This value is close to the expected value of 0.1 and it proves that the azafullerene enters the tubes with the same efficiency as C_{60}.

In Figure 31, we show the ESR spectra of the encapsulated mixture, (C_{59}N-der : C_{60})@SWCNT, after 700 °C vacuum annealing. The spectra of $C_{59}N:C_{60}$, a C_{59}N monomer embedded in C_{60},[104] is also shown for comparison. A triplet structure similar to that in $C_{59}N:C_{60}$ is observed in the heat-treated (C_{59} N-der : C_{60})@SWCNT overlapping with a broader line. The broader component is present in reference samples without encapsulated azafullerenes and is identified as a side-product. The broad line was numerically deconvoluted from the triplet component by fitting Lorentzian for all the signal. In Figure 31 a fit for the triplet component is shown with solid lines. However, the triplet pattern appears only after the 700 °C vacuum annealing. The ESR spectra of $C_{59}N:C_{60}$ is well understood:[104] at room temperature it consists of a triplet pattern due to the hyperfine interaction with the ^{14}N nucleus ($I = 1$) and a series of doublet peaks due to the interaction of the electron delocalized over the entire fullerene cage with ^{13}C nuclei ($I = 1/2$). The isotropic hyperfine coupling, $A_{\text{iso}} = 0.370(4)$ of the triplet pattern in (C_{59}N-der : C_{60})@SWCNT closely agree with those found for C_{59}N monomers in solvents $A_{\text{iso}} = 0.373$[108] and $A_{\text{iso}} = 0.37$[109] or $A_{\text{iso}} = 0.363(1)$ in the C_{60} matrix.[104] This proves that after the 700 °C heat treatment, a sizeable amount of rotating C_{59}N monomer radicals are present in the sample. This is not surprising in the view of the ability to form C_{59}N monomers from $(C_{59}N)_2$ dimers at similar temperatures,[110] however the current process is not reversible and the remnants of the side-groups are probably removed by the dynamic pumping. Although, the production of C_{59}N monomers inside SWCNTs was proved,[111] further work is required to understand the spectral details, to improve the background to triplet signal ratio, and in particular temperature dependent studies are required to study the tube properties.

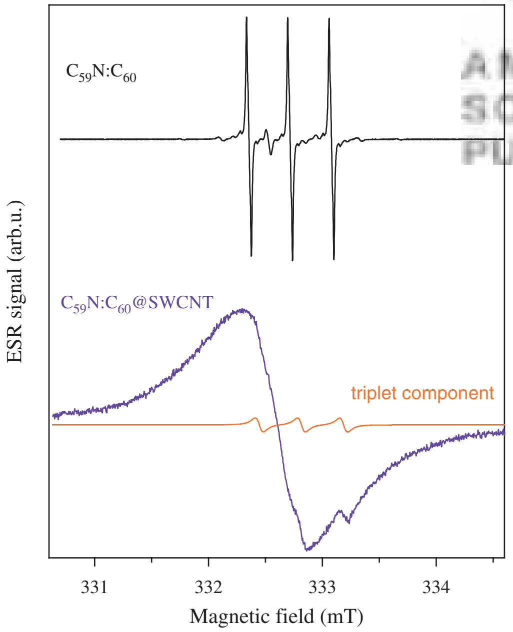

Fig. 31. ESR spectra of crystalline $C_{59}N:C_{60}$ (a) and ($C_{59}N:C_{60}$)@SWCNT obtained by annealing the (C_{59}N-der : C_{60})@SWCNT. A solid curve shows the triplet component after deconvolution from the total ESR signal.

4. SUMMARY

In summary, we reviewed how molecules encapsulated inside SWCNTs can be used to study various properties of the tubes themselves. Inner tubes grown from encapsulated fullerenes were shown to be an excellent probe of diameter dependent reactions on the outer tubes. Inner tubes grown from isotope labeled fullerenes and organic solvents allowed to understand the role of the different carbon phases in the growth of the inner tubes. In addition, isotope labeled inner tubes were shown to yield an unparalleled precision to study the density of states near the Fermi level using NMR. It was reviewed how magnetic fullerenes can be encapsulated inside SWCNTs yielding linear spin chains with sizeable spin concentrations and also to allow ESR studies of the tube properties.

Acknowledgments: This work was supported by the Austrian Science Funds (FWF) project Nr. 17345, by the Hungarian State Grants No. TS049881, F61733 and NK60984, by the EU projects HPRN-CT-2002-00192 and MERG-CT-2005-022103, and by the Zoltán Magyary postdoctoral fellowship. The author is particularly grateful to Hans Kuzmany and Rudolf Pfeiffer for their participation in the discussed works, for the stimulating discussions and for the critical comments on the manuscript. Á. Kukovecz, Z. Kónya, T. Pichler, H. Rauf, C. Kramberger, F. Hasi, E. Obraztsova, H. Alloul, P. M. Singer, J. Bernardi, P. Wzietek, F. Fülöp, A. Rockenbauer, A. Jánossy, F. Hauke, A. Hirsch, V. N. Popov, V. Zólyomi, and J. Kürti are acknowledged for their participation in the reviewed works. Ch. Schaman is acknowledged for preparing some of the figures.

References and Notes

1. Sumio Iijima, *Nature*, 354, 56 **(1991)**.
2. Sumio Iijima and Toshinari Ichihashi, *Nature* 363, 603 **(1993)**.
3. D. S. Bethune, C. H. Kiang, M. S. DeVries, G. Gorman, R. Savoy, R. Beyers, *Nature* 363, 605 **(1993)**.
4. A. N. Obraztsov, I. Pavlovsky, A. P. Volkov, E. D. Obraztsova, A. L. Chuvilin, and V. L. Kuznetsov, *J. Vac. Sci. Techn. B*, 18, 1059 **(2000)**.
5. G. Z. Yue, Q. Qiu, B. Gao, Y. Cheng, J. Zhang, H. Shimoda, S. Chang, J. P. Lu, and O. Zhou, *Appl. Phys. Lett.* 81, 355 **(2002)**.

6. J. H. Hafner, C. L. Cheung, and C. M. Lieber, *Nature* 398, 761 **(1999)**.

7. Adrian Bachtold, Peter Hadley, Takeshi Nakanishi, and Cees Dekker, *Science* 294, 1317 **(2001)**.

8. W. Harneit, C. Meyer, A. Weidinger, D. Suter, and J. Twamley, *Phys. St. Solidi B* 233, 453 **(2002)**.

9. N. Hamada, S. Sawada, and A. Oshiyama, *Phys. Rev. Lett.* 68, 1579 **(1992)**.

10. R. Saito, G. Dresselhaus, and M. S. Dresselhaus, Physical Properties of Carbon Nanotubes, Imperial College Press **(1998)**.

11. D. Chattopadhyay, L. Galeska, and F. Papadimitrakopoulos, *J. Am. Chem. Soc.* 125, 3370 **(2003)**.

12. R. Krupke, F. Hennrich, H. von Lohneysen, and M. M. Kappes, *Science*, 301, 344 **(2003)**.

13. Z. H. Chen, X. Du, M. H. Du, C. D. Rancken, H. P. Cheng, and A. G. Rinzler, *Nano Lett.* 3, 1245 **(2003)**.

14. M. Zheng, A. Jagota, M. S. Strano, A. P. Santos, P. Barone, S. G. Chou, G. Diner, M. S. B. A. Dresselhaus, R. S. McLean, G. B. Onoa, G. G. Samsonidze, E. D. Semke, M. Usrey, and D. J. Walls, *Science* 302, 1545 **(2003)**.

15. Sergei M. Bachilo, Michael S. Strano, Carter Kittrell, Robert H. Hauge, Richard E. Smalley, and R. Bruce Weisman, *Science* 298, 2361 **(2002)**.

16. C. Fantini, A. Jorio, M. Souza, M. S. Strano, M. S. Dresselhaus, and M. A. Pimenta, *Phys. Rev. Lett.* 93, 147406 **(2004)**.

17. H. Telg, J. Maultzsch, S. Reich, F. Hennrich, and C. Thomsen, *Phys. Rev. Lett.* 93, 177401 **(2004)**.

18. R. Egger and A. O. Gogolin, *Nature* 79, 50825085 **(1997)**.

19. K. P. Bohnen, R. Heid, H. J. Liu, and C. T. Chan, *Phys. Rev. Lett.* 93, 245501–1–4 **(2004)**.

20. D. Connétable, G.-M. Rignanese, J.-C. Charlier, and X. Blase, *Phys. Rev. Lett.* 94, 015503–1–4 **(2005)**.

21. Sander J. Tans, Michel H. Devoret, Hongjie Dai, Andreas Thess, Richard E. Smalley, L. J. Geerligs, and Cees Dekker, *Nature* 386, 474 **(1997)**.

22. C. L. Kane and E. J. Mele, *Phys. Rev. Lett.* 90, 207401–1–4 **(2003)**.

23. Catalin D. Spataru, Sohrab Ismail-Beigi, Lorin X. Benedict, and Steven G. Louie, *Phys. Rev. Lett.* 92, 077402–1–4 **(2004)**.

24. Vasili Perebeinos, J. Tersoff, and Phaedon Avouris, *Phys. Phys. Lett.* 92, 257402–1–4 **(2004)**.

25. Vasili Perebeinos, J. Tersoff, and Phaedon Avouris, *Phys. Phys. Lett.* 94, 027402–1–4 **(2005)**.

26. M. Bockrath, D. H. Cobden, Jia Lu, A. G. Rinzler, R. E. Smalley, L. Balents, and P. L. McEuen, *Nature* 397, 598 **(1999)**.

27. H. Ishii, H. Kataura, H. Shiozawa, H. Yoshioka, H. Otsubo, Y. Takayama, T. Miyahara, S. Suzuki, Y. Achiba, M. Nakatake, T. Narimura, M. Higashiguchi, K. Shimada, H. Namatame, and M. Taniguchi, *Nature* 426, 540 **(2003)**.

28. H. Rauf, T. Pichler, M. Knupfer, J. Fink, and H. Kataura, *Phys. Rev. Lett.* 93, 096805–1–4 **(2004)**.

29. Feng Wang, Gordana Dukovic, Louis E. Brus, and Tony F. Heinz, *Science* 308, 838 **(2005)**.

30. J. Maultzsch, R. Pomraenke, S. Reich, E. Chang, D. Prezzi, A. Ruini, E. Molinari, M. S. Strano, C. Thomsen, and C. Lienau, *Phys. Rev. B* 72, 241402 **(2005)**.

31. Brian W. Smith, Marc Monthioux, and David E. Luzzi, *Nature* 396, 323 **(1998)**.

32. B. W. Smith, M. Monthioux, and D. E. Luzzi, *Chem. Phys. Lett.* 315, 31 **(1999)**.

33. H. Kataura, Y. Maniwa, T. Kodama, K. Kikuchi, K. Hirahara, K. Suenaga, S. Iijima, S. Suzuki, Y. Achiba, and W. Krätschmer, *Synthetic Met.* 121, 1195 **(2001)**.

34. B. W. Smith and D. E. Luzzi, *Chem. Phys. Lett.* 321, 169 **(2000)**.

35. S. Bandow, M. Takizawa, K. Hirahara, M. Yudasaka, and S. Iijima, *Chem. Phys. Lett.* 337, 48 **(2001)**.

36. J. L. Hutchison, N. A. Kiselev, E. P. Krinichnaya, A. V. Krestinin, R. O. Loutfy, A. P. Morawsky, V. E. Muradyan, E. D. Obraztsova, J. Sloan, S. V. Terekhov, and D. N. Zakharov, *Carbon* 39, 761 **(2001)**.

37. Wencai Ren, Feng Li, Jian Chen, Shuo Bai, and Hui-Ming Cheng, *Chem. Phys. Lett.* 359, 196 **(2002)**.

38. R. Pfeiffer, H. Kuzmany, Ch. Kramberger, Ch. Schaman, T. Pichler, H. Kataura, Y. Achiba, J. Kürti, and V. Zólyomi, *Phys. Rev. Lett.* 90, 225501–1–4 **(2003)**.

39. M. Yudasaka, K. Ajima, K. Suenaga, T. Ichihashi, A. Hashimoto, and S. Iijima, *Chem. Phys. Lett.* 380, 42 **(2003)**.

40. F. Simon, H. Kuzmany, H. Rauf, T. Pichler, J. Bernardi, H. Peterlik, L. Korecz, F. Fülöp, and A. Jánossy, *Chem. Phys. Lett.*, 383, 362 **(2004)**.

41. M. Monthioux and L. Noé, Room temperature synthesis of C_{60}@SWNT (peapods). in XVIIIth International Winterschool on Electronic Properties of Novel Materials, *AIP Proceedings* **(2004)**.

42. A. N. Khlobystov, D. A. Britz, J. W. Wang, S. A. O'Neil, M. Poliakoff, and G. A. D. Briggs, *J. Mat. Chem.* 14, 2852 **(2004)**.

43. T. Pichler, H. Kuzmany, H. Kataura, and Y. Achiba, *Phys. Rev. Lett.* 87, 267401–1–4 **(2001)**.

44. F. Simon, Á. Kukovecz, Z. Kónya, R. Pfeiffer, and H. Kuzmany, *Chem. Phys. Lett.*, 413, 506 **(2005)**.

45. B. C. Liu, S. C. Lyu, S. I. Jung, H. K. Kang, C.-W. Yang, J. W. Park, C. Y. Park, and C. J. Lee, *Chem. Phys. Lett.* 383, 104 **(2004)**.

46. Masatoshi Abe, Hiromichi Kataura, Hiroshi Kira, Takeshi Kodama, Shinzo Suzuki, Yohji Achiba, Ken-ichi Kato, Masaki Takata, Akihiko Fujiwara, Kazuyuki Matsuda, and Yutaka Maniwa, *Phys. Rev. B* 68, 041405(R) **(2003)**.

47. V. Zólyomi and J. Kürti, *Phys. Rev. B* 70, 085403–1–8 **(2004)**.

48. M. Endo, H. Muramatsu, T. Hayashi, Y. A. Kim, M. Terrones, and M. S. Dresselhaus, *Nature*, 433, 476 **(2005)**.

49. F. Simon, Á. Kukovecz, C. Kramberger, R. Pfeiffer, F. Hasi, H. Kuzmany, and H. Kataura, *Phys. Rev. B* 71, 165439–1–5 **(2005)**.

50. H. Kuzmany, Solid-State Spectroscopy, An Introduction, Springer Verlag, Berlin **(1998)**.

51. F. Simon, Ch. Kramberger, R. Pfeiffer, H. Kuzmany, V. Zólyomi, J. Kürti, P. M. Singer, and H. Alloul, *Phys. Rev. Lett.* 95, 017401–1–4 **(2005)**.

52. J. Kürti, G. Kresse, and H. Kuzmany, *Phys. Rev. B* 58, R8869 **(1998)**.

53. R. Pfeiffer, H. Kuzmany, F. Simon, S. N. Bokova, and E. Obraztsova, *Phys. Rev. B*, 71, 155409–1–8 **(2005)**.

54. R. Pfeiffer, H. Kuzmany, T. Pichler, H. Kataura, Y. Achiba, M. Melle-Franco, and F. Zerbetto, *Phys. Rev. B* 69, 035404 **(2004)**.

55. R. Pfeiffer, F. Simon, H. Kuzmany, and V. N. Popov, *Phys. Rev. B* 72, 161404–1–4 **(2005)**.

56. M. S. Dresselhaus, G. Dresselhaus, and Ph. Avouris, Carbon Nanotubes: Synthesis, Structure, Properties, and Applications, Springer, Berlin, Heidelberg, New York **(2001)**.

57. H. Kataura, Y. Kumazawa, Y. Maniwa, I. Umezu, S. Suzuki, Y. Ohtsuka, and Y. Achiba, *Synthetic Met.* 103, 2555 **(1999)**.

58. R. Pfeiffer, Ch. Kramberger, F. Simon, H. Kuzmany, V. N. Popov, and H. Kataura, *Eur. Phys. J. B* 42, 345 **(2004)**.

59. V. N. Popov and Luc Henrard, *Phys. Rev. B* 65, 235415 **(2002)**.

60. Jian Ping Lu, X.-P. Li, and Richard M. Martin, *Phys. Rev. Lett.* 68, 1551 **(1992)**.

61. Valentin N. Popov, *New J. Phys.* 6, 17 **(2004)**.

62. U. D. Venkateswaran, D. L. Masica, G. U. Sumanasekera, C. A. Furtado, U. J. Kim, and P. C. Eklund, *Phys. Rev. B* 68, 241406(R), **(2003)**.

63. J. Wu, W. Walukiewicz, W. Shan, E. Bourret-Courchesne, J. W. Ager III, K. M. Yu, E. E. Haller, Kyle Kissell, Sergei M. Bachilo, R. Bruce Weisman, Richard E. Smalley, *Phys. Rev. Lett.* 93, 017404 **(2004)**.

64. A. Jorio, R. Saito, J. H. Hafner, C. M. Lieber, M. Hunter, T. McClure, G. Dresselhaus, and M. S. Dresselhaus, *Phys. Rev. Lett.* 86, 1118 **(2001)**.

65. Andreas Thess, Roland Lee, Pavel Nikolaev, Hongjie Dai, Pierre Petit, Jerome Robert, Chunhui Xu, Young Hee Lee, Seong Gon Kim, Andrew G. Rinzler, Daniel T. Colbert, Gustavo E. Scuseria, David Tománek, John E. Fischer, and Richard E. Smalley, *Science*, 273, 483 (**1996**).

66. H. Kuzmany, W. Plank, M. Hulman, Ch. Kramberger, A. Grüneis, Th. Pichler, H. Peterlik, H. Kataura, and Y. Achiba, *Eur. Phys. J. B* 22, 307 (**2001**).

67. Ch. Kramberger, R. Pfeiffer, H. Kuzmany, V. Zólyomi, and J. Kürti, *Phys. Rev. B*, 68, 235404 (**2003**).

68. M. Melle-Franco, H. Kuzmany, and F. Zerbetto, *J. Phys. Chem. B* 109, 6986 (**2003**).

69. S. Berber, Y.-K. Kwon, and D. Tománek, *Phys. Rev. Lett.* 88, 185502 (**2002**).

70. M. Otani, S. Okada, and A. Oshiyama, *Phys. Rev. B* 68, 125424–1–8 (**2003**).

71. Brian W. Smith and David E. Luzzi, *Chem. Phys. Lett.* 321, 169 (**2000**).

72. X. Liu, T. Pichler, M. Knupfer, M. S. Golden, J. Fink, H. Kataura, Y. Achiba, K. Hirahara, and S. Iijima, *Phys. Rev. B* 65, 045419–1–6 (**2002**).

73. F. Hasi, F. Simon, and H. Kuzmany, *J. Nanosci. Nanotechnol.* 5, 1785 (**2005**).

74. Y. Zhao, B. I. Yakobson, and R. E. Smalley, *Phys. Rev. Lett.* 88, 185501–1–4 (**2002**).

75. S. W. Han, M. Yoon, S. Berber, N. Park, E. Osawa, J. Ihm, and D. Tománek, *Phys. Rev. B* 70, 113402–1–4 (**2004**).

76. J. Bardeen, L. N. Cooper, and J. R. Schrieffer, *Phys. Rev.* 108, 1175 (**1957**).

77. F. Simon and H. Kuzmany, *Chem. Phys. Lett.* 425, 85 (**2006**).

78. G. Kresse and D. Joubert, *Phys. Rev. B* 59, 17581775 (**1999**).

79. X.-P. Tang, A. Kleinhammes, H. Shimoda, L. Fleming, K. Y. Bennoune, S. Sinha, C. Bower, O. Zhou, and Y. Wu, *Science* 288, 492 (**2000**).

80. C. Goze-Bac, S. Latil, P. Lauginie, V. Jourdain, J. Conard, L. Duclaux, A. Rubio, and P. Bernier, *Carbon* 40, 1825 (**2002**).

81. F. Simon, R. Pfeiffer, C. Kramberger, M. Holzweber, and H. Kuzmany, The Raman Response of Double Wall Carbon Nanotubes, Springer, New York (**2005**), pp. 203–224.

82. J. Kürti, V. Zólyomi, M. Kertész, and S. Guangyu, *New. J. Phys.* 5, 125.1–125.21 (**2003**).

83. M. A. L. Marques, M. d'Avezac, and F. Mauri, Magnetic response of carbon nanotubes from ab initio calculations howpublished = cond-mat/0510197.

84. P. M. Singer, P. Wzietek, H. Alloul, F. Simon, and H. Kuzmany, *Phys. Rev. Lett.* 95, 236403–1–4 (**2005**).

85. C. P. Slichter, Principles of Magnetic Resonance, 3rd edn. 1996, Spinger-Verlag, New York (**1989**).

86. H. Shimoda, B. Gao, X. P. Tang, A. Kleinhammes, L. Fleming, Y. Wu, and O. Zhou, *Phys. Rev. Lett.* 88, 15502 (**2002**).

87. A. Kleinhammes, S.-H. Mao, X.-J. Yang, X.-P. Tang, H. Shimoda, J. P. Lu, O. Zhou, and Y. Wu, *Phys. Rev. B* 68, 75418–1–6 (**2003**).

88. S. Okada and A. Oshiyama, *Phys. Rev. Lett.* 91, 216801–1–4 (**2003**).

89. C. L. Kane and E. J. Mele, *Phys. Rev. Lett.* 78, 1932 (**1997**).

90. J. W. Mintmire and C. T. White, *Phys. Rev. Lett.* 81, 2506 (**1998**).

91. T. Moriya, *J. Phys. Soc. Jpn.* 18, 516 (**1963**).

92. Jian Ping Lu, *Phys. Rev. B* 74, 1123 (**1995**).

93. H. Yoshioka, *J. Phys. Chem. Solids.* 63, 1281 (**2002**).

94. A. S. Claye, N. M. Nemes, A. Jánossy, and J. E. Fischer, *Phys. Rev. B* 62, 4845 (**2000**).

95. J.-P. Salvetat, T. Fehér, C. LHuillier, F. Beuneu, and L. Forró, *Phys. Rev. B* 72, 075440-1-6 (**2005**).

96. T. Almeida Murphy, Th. Pawlik, A. Weidinger, M. Höhne, R. Alcala, and J.-M. Spaeth, *Phys. Rev. Lett.* 77, 1075 (**1996**).

97. M. Waiblinger, K. Lips, W. Harneit, A. Weidinger, E. Dietel, and A. Hirsch, *Phys. Rev. B* 64, 159901–1–4 (**2001**).

98. B. Pietzak, M. Waiblinger, T. A. Murphy, A. Weidinger, M. Hohne, E. Dietel, and A. Hirsch, *Chem. Phys. Lett.* 279, 259 (**1997**).

99. A. Jánossy, S. Pekker, F. Fülöp, F. Simon, and G. Oszlányi, in *Proceedings of the IWEPNM* (**2000**), p. 199.

100. K.-P. Dinse, *Phys. Chem. Chem. Phys.* 4, 5442 (**2002**).

101. J. C. Hummelen, B. Knight, J. Pavlovich, R. Gonzalez, and F. Wudl, *Science* 269, 1554 (**1995**).

102. J. C. Hummelen, C. Bellavia-Lund, and F. Wudl, Heterofullerenes, Springer, Berlin, Heidelberg (**1999**), Vol. 199, p. 93.

103. M. J. Butcher, F. H. Jones, P. H. Beton, P. Moriarty, B. N. Cotier, M. D. Upward, K. Prassides, K. Kordatos, N. Tagmatarchis, F. Wudl, V. Dhanak, T. K. Johal, C. Crotti, C. Comicioli, and C. Ottaviani, *Phys. Rev. Lett.* 83, 3478 (**1999**).

104. F. Fülöp, A. Rockenbauer, F. Simon, S. Pekker, L. Korecz, S. Garaj, and A. Jánossy, *Chem. Phys. Lett.* 334, 223 (**2001**).

105. F. Simon, H. Kuzmany, J. Bernardi, F. Hauke, and A. Hirsch, *Carbon* 44, 1958 (**2006**).

106. A. Hirsch and B. Nuber, *Acc. Chem. Res.* 32, 795 (**1999**).

107. H. Kuzmany, W. Plank, J. Winter, O. Dubay, N. Tagmatarchis, and K. Prassides, *Phys. Rev. B* 60, 1005 (**1999**).

108. K. Hasharoni, C. Bellavia-Lund, M. Keshavarz-K, G. Srdanov, and F. Wudl, *J. Am. Chem. Soc.* 119, 11128 (**1997**).

109. A. Gruss, K.-P. Dinse, A. Hirsch, B. Nuber, and U. Reuther, *J. Am. Chem. Soc.* 119, 8728 (**1997**).

110. F. Simon, D. Arčon, N. Tagmatarchis, S. Garaj, L. Forró, and K. Prassides, *J. Phys. Chem. A.* 103, 6969 (**1999**).

111. F. Simon, H. Kuzmany, B. Náfrádi, T. Fehér, L. Forró, F. Fülöp, A. Jánossy, L. Korecz, A. Rockenbauer, F. Hauke, and A. Hirsch, *Phys. Rev. Lett.*, (in press).

Received: 28 March 2006. Revised/Accepted: 13 June 2006.